UNIVERSIDADE D
COIMBRA

Sérgio Manuel Domingues Melendre

NUMERICAL MODELLING OF FLOW PAST PHOTOVOLTAIC PANELS

Dissertação no âmbito do mestrado em Engenharia Mecânica, no ramo de Energia e Ambiente orientada pelo Professor Doutor Almerindo Domingues Ferreira e Professor Pedro Miguel Martins de Brito e apresentada ao Departamento de Engenharia Mecânica da Faculdade de Ciências e Tecnologia da Universidade de Coimbra

julho de 2023

FACULDADE DE CIÊNCIAS E TECNOLOGIA
UNIVERSIDADE D COIMBRA

Numerical modelling of flow past photovoltaic panels

A dissertation submitted in partial fulfillment of the requirements for the degree of Master in Mechanical Engineering in the speciality of Energy and Environment

Modelação computacional do escoamento em torno de painéis fotovoltaicos

Author

Sérgio Manuel Domingues Melendre

Advisors

Almerindo Domingues Ferreira

Pedro Miguel Martins Brito

Jury

President	**Professor Doutor Pedro de Figueiredo Vieira Carvalheira** Professor Associado da Universidade de Coimbra
Vowel	**Professor Doutor António Manuel Gameiro Lopes** Professor Associado da Universidade de Coimbra
Advisor	**Professor Pedro Miguel Martins Brito** Professor Assistente Convidado da Universidade de Coimbra

Coimbra, July, 2023

"Climb mountains not so the world can see you, but so you can see the world."

David McCullough Jr.

To my family.

Agradecimentos

A realização deste trabalho só foi conseguida devido ao apoio incondicional de algumas pessoas às quais dedico umas palavras de agradecimento.

Aos meus orientadores, Professor Almerindo Ferreira e Professor Pedro Brito, pela ajuda, motivação, disponibilidade, conhecimento transmitido ao longo do semestre e por terem disponibilizado o equipamento essencial para a execução da dissertação.

A todos os docentes do DEM que contribuíram para a minha formação académica.

Aos meus grandes amigos que me acompanharam em Coimbra, Júlia Taborda, Teresa Abreu, Francisco Félix, Tiago Carvalho, Tiago Vidas e Tomás Oliveira pelos momentos partilhados, pelo apoio, conversas e gargalhadas, por este grupo tão unido que formamos quase desde os primeiros dias no DEM.

À Josefa Guerra e ao Ricardo Agostinho que me acompanham desde antes de ter começado este curso pela amizade e por estarem sempre presentes.

Aos meus pais, ao meu irmão e avós, por todo o apoio, por todo o carinho e compreensão que sempre tiveram comigo.

A mi restante familia, que, a pesar de la distancia, me han transmitido todo su apoyo, cariño y ánimo en esta etapa tan importante de mi vida. Gracias.

A todos, um muito obrigado!

Abstract

In order to reduce the lifecycle cost of photovoltaic panels and mitigate destruction risks, understanding the relationship between the flow and the associated aerodynamic loading is a crucial step.

Computational fluid dynamics (CFD) is employed to study the flow around ground-mounted, standalone PV panels and to evaluate the mean wind load. Three tilt angles are studied (25º, 30º and 40º) as well as three wind incident directions (0º, 30º and 180º). The flow was simulated by following both two-dimensional and three-dimensional approaches employing Large Eddy Simulation and Reynolds-Average-Navier-Stokes methods, respectively. The numerical prediction results are compared with wind tunnel data available in the literature.

It was observed that for head-on wind direction, pressure distribution is approximately symmetric about the mid-lane of the panel on both upper (sun-facing) and lower (ground-facing) surfaces and that the maximum wind load, and thus, the resultant force, increased with higher tilt angles. For a wind direction of 30º, the pressure distribution is no longer symmetrical, having maximum positive values on the leading edge and largest negative values on the opposite edge. Moreover, the numerical prediction, both LES and RANS showed a reasonable agreement when compared with the experimental data.

CFD proved the capacity to integrate the design process of solar parks/farms, with the three-dimensional approach being more attractive as it allows to investigate a wider range of factors that have a direct impact on wind loads. Regarding the numerical turbulence methods, there is a good compromise between the accuracy of the results, execution time and computational resources when performing RANS instead of LES.

Keywords: CFD, Wind loads, Photovoltaic panels, RANS, LES, Pressure distribution.

Resumo

De forma a reduzir o custo total do dimensionamento das estruturas e mitigar o risco de destruição pela ação do vento, compreender a relação entre o escoamento e a respetiva carga aerodinâmica nos painéis fotovoltaicos é uma etapa fulcral.

A mecânica dos fluidos computacional (CFD) é utilizada para estudar o escoamento, o respetivo campo de pressão e a força resultante em painéis fotovoltaicos que se encontram montados próximo do solo. Três diferentes ângulos de inclinação foram estudados (25º, 30º e 40º) tal como três direções de escoamento (0º, 30º 180º). O escoamento foi estudado recorrendo a simulações em duas dimensões e três dimensões por meio de simulações do tipo Large Eddy Simulation e Reynolds-Average-Navier-Stokes. Os resultados da previsão computacional são comparados com dados experimentais obtidos em túnel de vento e que se encontram disponíveis na literatura.

Foi observado que quando o escoamento incidente ocorre na direção perpendicular ao lado maior do painel, a distribuição da pressão na parte da frente (voltada para o sol) e de trás (voltada para o solo) é parcialmente simétrica e que a força máxima exercida pela pressão, e consequentemente, a força resultante aumenta com o ângulo de inclinação. Para um ângulo de escoamento de 30º, a distribuição da pressão deixa de ser simétrica, apresentando os valores máximos de pressão positiva no bordo de ataque e valores negativos máximos no bordo oposto. Além disso, a previsão numérica, tanto LES como RANS demonstraram seguir a tendência dos resultados experimentais de forma razoável.

Em suma, CFD revela capacidade para integrar o projeto de dimensionamentos de parques solares, sendo que a abordagem tridimensional é mais atrativa, uma vez que permite investigar um leque mais amplo de fatores que têm impacto na força exercida pelo vento. Em relação aos modelos de turbulência, existe um bom compromisso entre a precisão dos resultados, o tempo de simulação e os recursos computacionais quando se implementa RANS em vez de LES.

Palavras-chave: CFD, Carga de vento, Painéis fotovoltaicos, RANS, LES, Distribuição da pressão.

Contents

LIST OF FIGURES

LIST OF TABLES

LIST OF SYMBOLS AND ACRONYMS

Symbols

α	Velocity profile power-law exponent	
α_t	Tilt angle	$^\circ$
β_1	Wilcox ω_{wall} model constant	
δ	Boundary layer thickness	m
δ_{ij}	Kronecker delta tensor	
τ_{ij}	Sub-grid scale stress tensor	
ϕ	Generic scalar variable	
$\bar{\phi}$	Time-averaged component of ϕ	
ϕ'	Instantaneous deviation from $\bar{\phi}$	
Δ	Filter width	
ε	Turbulent kinetic energy dissipation rate	m^2/s^3
θ	Wind direction angle	$^\circ$
λ	Eddy wavelength	m
μ	Dynamic viscosity	$Pa \cdot s$
ν	Kinematic viscosity	m^2/s
ν_{sgs}	Sub-grid scale eddy viscosity	m^2/s
ν_t	Kinematic eddy viscosity	m^2/s
ω	Specific dissipation rate of turbulent kinetic energy	$1/s$
ω_{wall}	Near-wall value of ω	$1/s$

A	Reference area	m^2
Co	Courant number	
C_D	Drag coefficient	
C_L	Lift coefficient	
C_p	Pressure coefficient	
D	Entire domain	
E	Spectral energy	m^3/s^2
F	Resultant force	N
F_D	Drag	N
F_L	Lift	N
G	Filter function	
k	Turbulence kinetic energy	m^2/s^2
K_0	Kolmogorov constant	
L	Panel chord length	m
l	Length scale	m
p	Pressure	Pa
p_k	Kinematic pressure	m^2/s^2
Re	Reynolds number	
Re_l	Reynolds number of a ‘large eddy’	
$\overline{S}_{ij}$	Deformation tensor of the resolved field	
St	Strouhal number	
t	Time	s
t_1	Fluctuating field time scale	s

Δt	Time interval larger than t	s
Δt_{exec}	Total execution time of the simulation	h
Δt_s	Simulation time step	s
$\bar{u}_i$	Time-averaged velocity component in the i direction	m/s
$\bar{u}_j$	Time-averaged velocity component in the j direction	m/s
U_0	Freestream velocity	m/s
y^+	Dimensionless distance from the wall to the first cell-center	
Δy_1	Distance from the wall to the first cell-center	m

Acronyms

2D	Two-Dimensional
3D	Three-Dimensional
ABL	Atmospheric Boundary Layer
CAD	Computed Aided Design
CAE	Computed Aided Engineering
CFD	Computational Fluid Dynamics
DES	Detached Eddy Simulation
FDM	Finite Difference Method
FEM	Finite Element Method
FOAM	Field Operation Manipulation
FVM	Finite Volume method
HVAC	Heating, Ventilation and Air Conditioning
LE	Leading Edge
LES	Large Eddy Simulation
OBJ	Wavefront Object
PISO	Pressure-Implicit with Splitting of Operators
PV	Photovoltaic
RANS	Reynolds-Averaged Navier Stokes
RGN	Renormalized Group
SGS	Sub-grid Scale
SST	Shear Stress Transport
STL	Stereolithographic
TE	Trailing Edge

1. INTRODUCTION

The first chapter of this dissertation aims to motivate this study. Additionally, a short description of Computational Fluid Dynamics (CFD) as an important tool for many engineering branches is presented. The main objectives of the thesis, along with its structure, are also described to provide a clear overview of the coming chapters to the readers.

1.1. Motivation

The Sun is a major source of inexhaustible free energy for planet Earth. Theoretically, solar energy possesses the potential to adequately fulfill the energy demands of the entire world (Kabir et al., 2018).

The amount of energy provided by the Sun is staggering, enough to power the great oceanic and atmospheric currents. Earth's ultimate recoverable resource of oil, estimated at 3 trillion barrels contains $1.7 \times 10^{22}\ J$ of energy, which the Sun supplies to Earth in 1.5 days. The enormous power that the Sun continuously delivers to Earth, $1.2 \times 10^{5}\ TW$, dwarfs every other energy source, renewable or nonrenewable (Crabtree & Lewis, 2008).

Nowadays, the use of renewable energy technologies has an important role in the purpose of alleviating greenhouse gas emissions and fighting climate change. Photovoltaic (PV) or solar modules/panels are largely used as a renewable energy alternative for electricity production (sunlight is converted to electricity by exciting electrons in a solar cell). PV panels should collect energy non-stop throughout decades, regardless of severe wind speed episodes, for this reason, they are of particular interest in wind engineering. Furthermore, their vulnerability to wind loads is a major concern for both manufacturers and users since these structures are commonly installed in the form of large-scale power plants (Wittwer et al., 2022). Along with wind turbines, PV panels have been one of the most rapidly deployed renewable energy technology on the planet, spawning growing industries that are emerging in many regions of the world (Mazzucato, 2015). Notwithstanding, the employment of simplifications or insufficient knowledge at the design stage frequently leads to unsafe or costly results (Cao et al., 2013).

Hence, understanding the connection between the flow and the associated aerodynamic loading for PV panels is a fundamental step in reducing costs through appropriate sizing of structures, improved location selection criteria, and potential guidance for load mitigation via flow control. This is essential in photovoltaic installations since structural components represent about 30% of the total installation costs. (Pieris et al., 2022).

Figure 1.1. Solar power plant - also known as solar park/farm.

1.2. Use of Computational Fluid Dynamics

Computational Fluid Dynamics is a Computer Aided Engineering (CAE) technology that produces quantitative predictions of fluid flow, heat and mass transfer, chemical reactions, and related phenomena based on the conservation laws (conservation of mass, momentum, and energy) governing fluid motion (Hu, 2012).

This technology became an important tool in a wide range of industrial and non-industrial areas such as the aerodynamics of aircraft and vehicles, hydrodynamics of ships, power plants (*e.g.* combustion in gas turbines), electrical and electronic engineering (*e.g.* cooling of equipment including microcircuits), chemical process engineering (*e.g.* mixing and separation), biomedical engineering (*e.g.* blood flows through arteries and veins), the external and internal environment of buildings (*e.g.* wind loading and HVAC) and weather prediction (Versteeg & Malalasekera, 2007).

Sumner et al. (2010) also refer to CFD as a "virtual, multiscale wind tunnel" as it allows the investigation of a wide range of theoretical and practical problems. Additionally, it has the advantage of being infinitely scalable and providing field (rather than punctual) data when compared to wind tunnel experiments.

Apart from restrictions related to computation and data storage, another aspect that delayed the establishment of CFD is the fact that the governing equations to be solved, that is, the continuity equation (1.1) and the Navier-Stokes (Navier, 1823; Stokes, 1845) equations (1.2), are certainly complex. This differential equation system precisely models the flow phenomena, from laminar to turbulent, single, or multiphase, compressible, or incompressible flows.

$$\frac{D\rho}{Dt} + \rho\nabla\vec{V} = 0 \tag{1.1}$$

$$\rho\frac{D\vec{V}}{Dt} = -\nabla p + \rho\vec{g} + \mu\nabla^2\vec{V} \tag{1.2}$$

The Finite Difference Method (FDM), Finite Element Method (FEM) and Finite Volume Method (FVM) are the three principal numerical approaches in which CFD is based (Jeong & Seong, 2014). The FVM is a numerical technique that transforms the governing partial differential equations into discrete algebraic equations over finite volumes which form a computational grid (or mesh). Such transformation is performed by integrating the differential equations over each discrete element. Because the flux entering a given volume is identical to that leaving the adjacent volume, the FVM is strictly conservative. This intrinsic conservation property of the FVM makes it the preferred numerical method in CFD (Moukalled et al., 2016).

As stated in Versteeg & Malalasekera (2007), CFD codes typically contain three main elements:

1. Pre-processor: Pre-processing consists of the definition of the geometry of the region of interest, that is, the computational domain. Afterward, the mesh is generated and the physical and chemical phenomena that need to be modelled are selected followed by the definition of fluid properties and the specification of the boundary conditions;

2. Solver: the algorithms to compute the flow are implemented, the governing equations are transformed following the FVM and a solution for the algebraic equations is obtained through an iterative method;
3. Post-processor: once the data is obtained, it needs to be analyzed and visualized with the right tools.

1.3. Approach and Aims

The primary objective of this dissertation is to investigate the wind flow characteristics around PV panels through numerical modelling. Specifically, the study aims to predict the pressure field and calculate the resultant force generated by the flow.

To achieve this goal, the numerical analysis is carried out using OpenFOAM® (Open Field Operation and Manipulation), an open-source, finite volume code which is composed of a set of libraries written in C++ language along with the post-processing and visualization software ParaView®.

Therefore, this work aims to accomplish the following objectives:

i. Generate a quality mesh using OpenFOAM® utilities;
ii. Select a proper turbulence model for the case, according to the literature review;
iii. Perform a grid independence test to verify its adequacy;
iv. Validate the numerical results against experimental measurements and evaluate the accuracy of the numerical results.

1.4. Outline of the thesis

Considering the aforementioned points, the rest of the thesis consists of the following chapters:

- Chapter 2 gives a literature review of previous research exploring the wind loads and flow around photovoltaic panels and inclined flat plates, both experimental and numerical approaches are discussed.
- Chapter 3 presents an overview of turbulence and its modelling, starting with a brief explanation of turbulence itself. Then, a succinct description of the most common numeric turbulence models available in CFD is made.

- Chapter 4 presents the methodology used for both two-dimensional and three-dimensional CFD analysis performed in this dissertation, the implemented turbulence models, and the initial and boundary conditions.
- Chapter 5 presents the results of the numerical analysis. Also, there are comparisons between the numerical predictions against experimental results of flow around PV panels in order to validate the CFD methodology applied, and a discussion is performed.
- Chapter 6 show the conclusions of the current work.

2. LITERATURE REVIEW

In this chapter, the literature regarding the study of the flow around photovoltaic panels, as well as the wind loads, and their effects are presented. Firstly, some aerodynamic parameters are revised. Then, the flow and wind load on photovoltaic panels are described as documented by some researchers, based on both experimental and numerical results.

2.1. Aerodynamic Parameters

Regarding aerodynamic loading, there are quantities inherently more descriptive than the absolute aerodynamic forces and moments themselves. These are dimensionless pressure, force (lift and drag), and moment coefficients, defined as follows (Anderson, 2016):

- Pressure coefficient:

$$C_p = \frac{p - p_\infty}{\frac{1}{2}\rho {U_0}^2} \tag{2.1}$$

- Lift coefficient:

$$C_L = \frac{F_L}{\frac{1}{2}\rho {U_0}^2 A} \tag{2.2}$$

- Drag coefficient:

$$C_D = \frac{F_D}{\frac{1}{2}\rho {U_0}^2 A} \tag{2.3}$$

- Moment coefficient:

$$C_M = \frac{M}{\frac{1}{2}\rho {U_0}^2 A l} \tag{2.4}$$

Where ρ is the density, U_0 the freestream velocity, A the reference area, p is the pressure on the surface and p_∞ is the pressure in the freestream. Parallel and perpendicular aerodynamic forces regarding the wind direction are labelled as drag (F_D) and lift (F_L), respectively. Moreover, M is the moment or torque about the center axis with l being the reference length.

A free-body diagram of the applied forces and momentum that result from the wind flow on a PV panel (tilted flat plate) is shown in Figure 2.1.

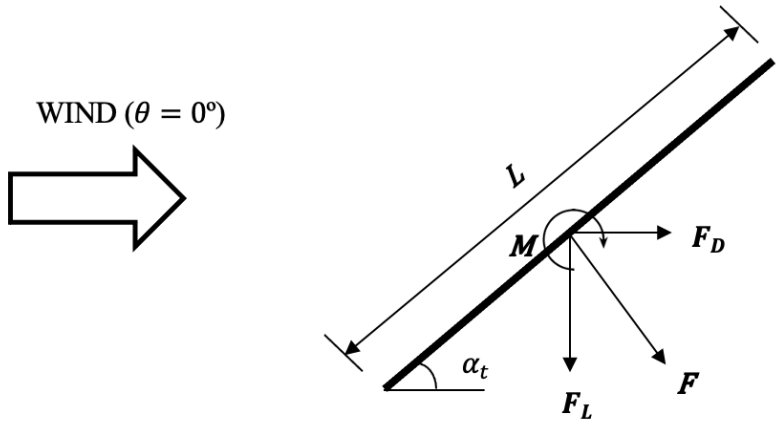

Figure 2.1. Aerodynamic forces on an inclined flat plate for a wind direction of 0º. Adapted from (Jubayer & Hangan, 2014)

It is important to refer that, for the representation of a flat plate with a tilt angle α_t, shown in Figure 2.1, the leading edge (LE), the part that first contacts the air, is the lower end of the plate, and the trailing edge (TE) is the upper end of the plate.

Regarding the pressure distribution, it varies according to the wind direction. For a wind direction (θ) of 0º the pressure is positive on the upper surface and negative (suction) on the lower surface. On the contrary, for a wind direction of 180º, the pressure is negative on the upper surface and negative on the lower one.

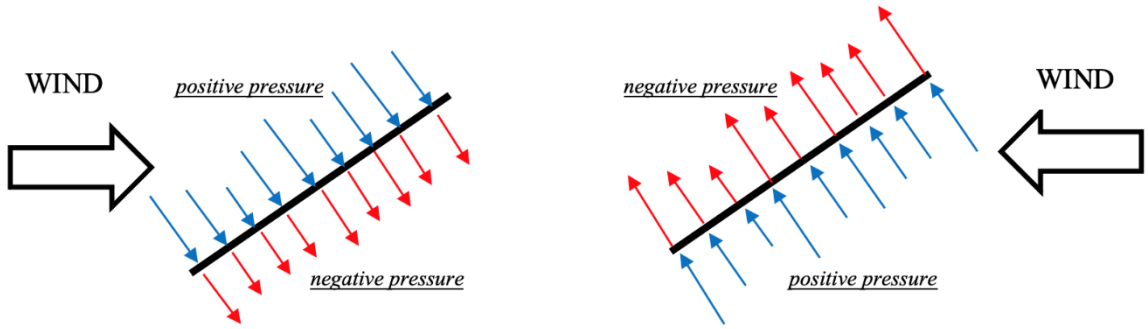

Figure 2.2. Flat plate pressure distribution according to the wind directions θ = 0º (left) and θ = 180º (right). Adapted from (Wittwer et al., 2022).

2.2. Flow and wind load on photovoltaic panels

In the available literature, one can find several studies that have been performed to estimate the wind loads on PV panels. Experimental studies, usually conducted in wind tunnels, can be split into two categories: roof-mounted and ground-mounted; wind tunnel testing of ground-mounted solar panels shows to be challenging, as this configuration brings up the problem of artificially simulating the lowest 10 m of the atmospheric boundary layer (ABL), the surface layer (Jubayer & Hangan, 2015). Among the latter group, it is possible to split it into two cases: isolated systems (Abiola-Ogedengbe et al., 2015; Shademan et al., 2014) and forming arrays (Strobel & Banks, 2014). In addition, more recently, even studies on floating PV panels have been performed (Cazzaniga et al., 2018; Choi et al., 2023).

The most common PV panels are rectangular-shaped flat plates that are inclined with a certain angle, determined by the latitude of the location, to capture the maximum amount of sunlight. The characteristics of the wind, such as its direction, speed, exposure conditions and the shape of the structure have an important impact on the nature of the force induced on the PV panel. (Abiola-Ogedengbe et al., 2015).

Perhaps one of the earliest studies regarding the flow of air on an inclined flat plate was carried out by (Fage & Johansen, 1927), in which the authors experimentally studied the pressure distribution over the front surface with angles of attack between 0 and 90º. It was observed that the normal force per unit length increases rapidly with the angle of attack until an angle of 9º and then falls slowly at 15º. Then, the force increases again to a maximum value at a 90º angle.

Wind tunnel tests performed by Pfahl et al., (2011) revealed that the wind load components vary significantly with the aspect ratio of solar trackers. The vertical distribution of the mean wind speed is frequently described using the power law approach, equation (2.5), common practice in wind engineering and, as a result, the preferred procedure in most of the studies presented in the present literature review.

$$\frac{u}{U_0} = \left(\frac{z}{\delta}\right)^{\alpha} \tag{2.5}$$

where U_0 is the freestream velocity, δ the boundary layer thickness and α the power law exponent.

The authors concluded that higher aspect ratios, *i.e.*, ratio between span and chord length, are advantageous for the different structural parts apart from the azimuth drive.

Cao et al., (2013) also carried out wind tunnel testing, using a model at a scale of 1:50, to evaluate the uplift wind load on solar panel arrays mounted on flat roofs. In a comparison between the single and multi-array cases, they noted that the most unfavourable module forces for single arrays are much larger than those for multi-arrays. One model was installed for the single-array cases whereas two identical models were installed for multi-array cases. In the case of two neighboring panels, the results show that both the mean and peak values of the two panels grow with the tilt angle from 15º to 45º, consequently, conclusion is that the larger the tilt angle, the higher the uplift wind loads on the solar panels. It was also noted that the most unfavourable module forces are much larger for standalone cases than those for multi-array. Moreover, panel-generated turbulence becomes greater with the increase of the distance between arrays which intensifies the module forces.

Stathopoulos et al., (2014) executed an experimental study to understand the wind pressure distribution on stand-alone panel surfaces and panels attached to flat building roofs. The results showed that the effect of wind direction is significant, being the 135º angle the most critical as both maximum and minimum peaks of pressure coefficients are found. In general, extreme values of pressure coefficient appear within the wind direction range between 105º and 180º.

Warsido et al., (2014) conducted experiments to comprehend the effects of spacing on the solar panel array. They found out that the first row provides a sheltering effect that decreases the mean forces coefficients on the following rows. The biggest reduction of wind loads coefficient was observed on the second row but then it dropped quickly afterwards. Also, the peak force and moment coefficients increase with the increase of longitudinal spacing since the sheltering effect is reduced. Moreover, they discovered that increasing the lateral spacing between array columns has minimal effect on the force and moment coefficients. However, the wind load coefficients increased as the longitudinal spacing between panel rows increased. Comparison of wind load coefficients of an isolated panel with the corresponding coefficients from the first-row panels of ground and roof-mounted arrays showed that isolated panels are subjected to higher wind loads than individual panels in a solar array.

The pressure field on the upper and lower surfaces of a standalone PV module was studied by (Abiola-Ogedengbe et al., 2015). Four different wind directions were tested in a wind tunnel. The authors concluded that the pressure distribution on the module surface is symmetric about its mid-plane for head-on wind (0º and 180º) and asymmetric for other wind directions. As expected, pressure magnitudes were found to be higher at larger tilt angles.

Wittwer et al., (2022) carried out experimental measurements, performing boundary layer tests in a wind tunnel, to determine the wind loads considering two situations: stand-alone and panel arrays. Uniform, smooth, and turbulent flows were used for the isolated model. An ABL (atmospheric boundary layer) flow was simulated with a mean velocity profile following the power law (as given by equation 2.5). Several wind directions were considered, from 0º to 180º at 15º intervals. The authors concluded that the pressure coefficient grow with the increase of the tilt angle. For the array of panels, the larger positive local net pressure effects correspond to a wind direction of 0º, and the greatest suction occurs with a wind direction of 135º. For the isolated module, it was observed that the greatest positive local net effects occur at a 45º wind direction and, in the same way as the array of panels, the strongest negative effects happen at a 135º wind direction.

Choi et al. (2022) measured the pressure distribution on every row of a solar panel array and concluded that peripheral panel rows had the highest drag and lift coefficients because they were the first encountered by the wind. Therefore, the middle rows were exposed to a smaller wind load due to the sheltering effect provided by the first windward row. This sheltering effect results in a gradual decrease of the lift and drag coefficient as the wind passes along the array.

Pieris et al. (2022) investigated the aerodynamics of flat plates in ground effect for aspect ratios of 1 and 2 and angles of attack between -90º and 90º. They observed that at sufficiently low free-flight pre-stall angles (angles that generate maximum lift), the increase in edge velocity at low gap ratios caused greater suction. The results of the study suggest that the loading increments are dependent on aspect ratio and orientation. Moreover, it was also noted that the ground effect has the most substantial influence on aerodynamic loads on inclined flat plates placed around the stall angle ($20º \leq \alpha_t \leq 40º$).

More recently, other researchers carried out numerical simulations to analyse with more detail the wind load characteristics of PV panels. To estimate the pressure between the lower surface of the PV panels and the surface from the roof, a numerical simulation using

the unsteady Bernoulli equation, in which the time histories of external pressure coefficients on the bare roof (roof with no PV panel) is used, was applied by (Uematsu et al., 2022).

Reina & De Stefano, (2017) employed CFD simulations considering two different modelling approaches, under ABL flow, which consists in simulating either the whole three-dimensional system or a reduced portion. The flow was simulated for various panel inclinations concerning the wind direction by using the Reynolds-Average-Navier-Stokes (RANS) approach, with the Shear Stress Transport (SST) k-ω turbulence model. It was noted that, for head-on wind ($\theta = 0^{o}$ and 180^{o}), the reduced model provides acceptable results, when compared to the fully three-dimensional solution, with a great benefit in terms of computational power and time.

Irtaza & Agarwal, (2018) simulated a solar array using the unsteady RANS equations together with the Renormalized Group (RGN) turbulence model to study the turbulent wind effect on PV panels. The authors observed that the maximum wind pressure when $\theta = 0^{o}$ and $\theta = 180^{o}$. Later PV array (both ground-mounted and roof-mounted) with tilt angles varying from 10^{o} to 60^{o} revealed that the net pressure coefficient analysed in the unsteady RGN k-ε turbulence model increased along with the array tilt angle.

Shademan et al., (2014) carried out Detached Eddy Simulation (DES) to investigate the unsteady wind loading on solar panels as well as the influence of ground clearance. It was shown that the mean flow field past a PV panel is substantially dependent on ground clearance. An increase in ground clearance results in a greater mean wind loading as the stagnation pressure and the mean pressure difference between the surfaces of the panel raise. Moreover, stronger vortex shedding and larger unsteady forces on the panel were demonstrated with the increase in ground clearance.

Wang et al., (2020) conducted Large Eddy Simulation (LES) to evaluate the wind pressure and force coefficients of solar arrays mounted on a flat roof building under two normal wind directions (0^{o} and 180^{o}). The analysis revealed that when wind attacks from the lower edges of the solar panel, *i.e.*, with an angle of 0^{o}, the reverse wind in the recirculation region flows towards the upper surface of upstream PV panels and local separation occurs at the higher edges. As a result, larger negative mean pressures are induced on the lower surface than the upper one.

2.3. Remarks

The studies reviewed in this literature review demonstrate the dynamic nature of the wind loads on PV panels, which depend on various factors, such as the panel tilt angle, aspect ratio, if they are ground-mounted or roof-mounted, wind direction, ground clearance, and the configuration of the panel array.

While experimental studies have provided valuable insights on the wind loads on PV panels due to the flow, recent numerical simulations have allowed a more detailed analysis of the pressure distribution on these structures.

3. TURBULENCE MODELLING

Turbulence is a prevalent phenomenon in many engineering applications, hence it is an important aspect of studying the effects of wind on PV panels. In this chapter, a brief overview on the concept of turbulence and the models that capture, to a sufficient degree of detail, are explored.

3.1. A succinct description of the concept of turbulence

Turbulence is a phenomenon that occurs frequently in nature, as a result, it has been the subject of study for several centuries (Piomelli, 1999). It can be defined as the swirling motion of fluids that occurs irregularly in space and time (Sreenivasan, 1999). One of the fundamental aspects of this phenomenon is that it is always three-dimensional and unsteady with a large range of scale motions (Zhiyin, 2015).

Turbulent flow is the usual state of fluid motion at high Reynolds numbers, a dimensionless parameter that represents the ratio of inertial forces to viscous forces, described in equation (3.1):

$$Re = \frac{\rho_0 U_0 l}{\mu} \tag{3.1}$$

where (μ) is the dynamic viscosity of the fluid and (l) the characteristic dimension.

This implies that, at very high Reynolds numbers, viscous effects are no longer important, thus, many aspects of turbulent flow can be described without considering viscosity. Inherent in all thinking about turbulence is the concept of an eddy, whose interpretation is often based on analogies with simpler swirling motions such as those associated with vortices (Smits, 2009). These rotational flow structures have a wide range of length scales. The characteristic velocity (v) and characteristic length (l) of the larger eddies are of the same order of the velocity scale (U_0) and length scale (l_s) of the mean flow. Therefore, a 'large eddy' Reynolds number, given by equation (3.2), is not very different in magnitude from $\rho_0 U_0 l/\mu$ *(*equation (3.1)*).*

$$Re_l = \frac{\rho_0 v l_s}{\mu} \tag{3.2}$$

As a result, these large eddies are dominated by inertia effects and viscous effects are negligible, and hence inviscid. The largest turbulent eddies interact with and extract energy from the mean flow, with the conservation of the angular momentum, a process called vortex stretching. This causes the rotation rate to increase and the radius of their cross-section to decrease. The stretching work done by the mean flow on the large eddies during this event provides the energy which maintains the turbulence. Smaller eddies are stretched strongly by larger eddies and feebly with the mean flow. Thus, the kinetic energy is transferred from large eddies to gradually smaller and smaller eddies; this is the definition of energy cascade.

The spectral energy $E(k)$ is shown as a function of the wavenumber $k = 2\pi/\lambda$, where λ is the wavelength of the eddies. The diagram shows that the energy content peaks at low wavenumber, thus the large eddies are the ones that contain more energy. As the wavenumber increases, the spectral energy rapidly decreases, so the smallest eddies have the lowest energy content (Versteeg & Malalasekera, 2007).

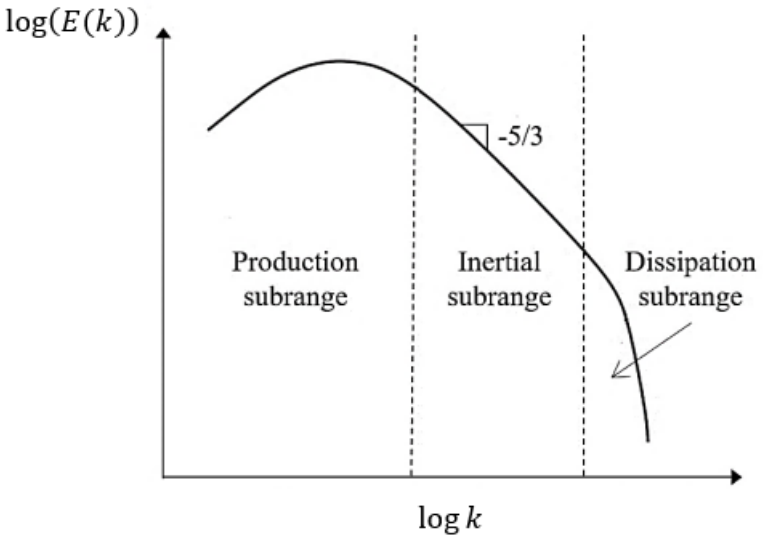

Figure 3.1. Energy spectrum as a function of the wavenumber (Kolmogorov, 1941).

The spectrum shown in Figure 3.1 is divided into three ranges: the production subrange (low wavenumber), the inertial subrange (intermediate wavenumber) and the dissipation subrange (high wavenumber) (Smits, 2009).

Kolmogorov (according to Versteeg & Malalasekera, 2007) argued that the structure of the smallest eddies, and thus, their spectral energy should only depend on the rate of

dissipation of turbulent energy (ε) and the kinematic viscosity of the fluid (ν)(Versteeg & Malalasekera, 2007).

Therefore, and by dimensional analysis:

$$E = E(k, \varepsilon, \nu) \tag{3.3}$$

$$[E] = \frac{L^3}{T^2} \tag{3.4}$$

$$[\varepsilon] = \frac{L^2}{T^3} \tag{3.5}$$

$$[\nu] = \frac{L^2}{T} \tag{3.6}$$

$$[k] = \frac{1}{L} \tag{3.7}$$

However, in the inertial subrange, the energy should be independent of ν. Hence, once again, by dimensional analysis:

$$\frac{E(k)}{\varepsilon^{2/3} k^{-5/3}} = K_0 = Kolmogorov\ constant \approx 1.44 \tag{3.8}$$

That is:

$$E(k) = \varepsilon^{2/3} k^{-5/3} K_0 \tag{3.9}$$

This famous result is known as the Kolmogorov (1941) -5/3 law (Smits, 2009).

3.2. Numerical turbulence methods

Turbulence modelling can be defined as the employment of mathematical models to predict the effects of turbulence. Depending on the method, one can obtain different levels of precision with corresponding computational costs. In this subchapter, Direct Numerical Simulation (DNS), Reynolds-Average-Navier-Stokes (RANS) and Large Eddy Simulation (LES) are introduced.

3.2.1. Direct Numerical Simulation

DNS approaches simulate turbulent flows in time and space directly. As a result, they represent the most precise simulation method: The Navier-Stokes equations are solved without approximating the turbulent quantities by a sum between the time average and fluctuations. With this method, any approximation is avoided. Thus, all the possible details

of the flow in space and time are obtained and their results are equivalent to an experiment in a laboratory, but in this case, without any intrusive technique (Hami, 2021).

To achieve this degree of precision a very fine mesh captures all the scales that are present in a given flow, from the smallest to the largest eddies. Therefore, DNS is very expensive in terms of computational resources, and it can be applied only to low Reynolds number flows over simple geometry (Zhiyin, 2015).

3.2.2. Reynolds-Average-Navier-Stokes

In some cases, one is mainly interested in the steady-state fluid flow, hence simulating the detailed instantaneous flow is unnecessary. This method leads to a great reduction in computational time. This is the basis of RANS, an approach in which one solves only for the averaged quantities while the effect of all the scales of instantaneous turbulent motion is modelled by a turbulence model (Zhiyin, 2015). Fluid mechanics are governed microscopically by the Navier-Stokes equations from the usual conservation principles of mechanics: conservation of mass and momentum. In the aerodynamic and low altitude wind context, these equations are simplified: incompressible flow, air temperature is constant, and air will be considered a Newtonian fluid (Hami, 2021).

The turbulent motion as an arbitrary fluctuation around the mean value of a scalar variable (ϕ), where ($\bar{\phi}$) is the mean value and (ϕ') the instantaneous deviation component is given by the Reynolds decomposition, equation (3.10).

$$\phi = \bar{\phi} + \phi' \tag{3.10}$$

The value of $\bar{\phi}$ can be given by equation (3.11), where Δt is a time interval much larger than the fluctuation time scale (t_1) (Markatos, 1986). Oliveira & Lopes, (2016) suggest that Δt 5 seconds greater can be sufficient in several cases.

$$\bar{\phi} = \lim_{t\to\infty} \frac{1}{\Delta t} \int_{t}^{t+\Delta t} \phi dt \tag{3.11}$$

Substituting the equation into the continuity and the Navier-Stokes equations one derives equations (3.12) and (3.13), respectively:

$$\frac{\partial \bar{u}_i}{\partial x_i} = 0 \tag{3.12}$$

$$\frac{\partial \bar{u}_i}{\partial t} + \frac{\partial}{\partial x_j}\left(\bar{u}_i \bar{u}_j\right) = -\frac{1}{\rho}\frac{\partial \bar{p}}{\partial x_i} + \nu \frac{\partial^2 \bar{u}_i}{\partial x_j x_j} - \frac{\partial}{\partial x_i}\left(\overline{u_i{}' u_j{}'}\right) \tag{3.13}$$

The latter equation is known as the RANS equation which gives rise to the so-called kinematic Reynolds stresses, defined as the tensor $\overline{u_i{}' u_j{}'}$. The Reynolds stresses depend on the velocity fluctuations $u_i{}'$, and introduce new unknown quantities in the RANS equations and, as a result, these equations no longer constitute a closed system. Further equations describing the relationship between $\overline{u_i{}' u_j{}'}$ are needed to close the system of equations, this is known as the closure problem in turbulence modelling. Approximating the Reynolds stress components by analogy with a Newtonian type of linear constitutive relationship between the turbulence stress and the mean strain-rate tensor is one of the simplest turbulence models for $\overline{u_i{}' u_j{}'}$. This model uses the so called Boussinesq eddy-viscosity approximation, given by the following equation:

$$\overline{u_i{}' u_j{}'} = \frac{2}{3} k \delta_{ij} - \nu_t \left(\frac{\partial \bar{u}_i}{\partial x_j} + \frac{\partial \bar{u}_j}{\partial x_i} \right) \tag{3.14}$$

where ν_t is the kinematic eddy viscosity, $k \equiv \frac{1}{2}\overline{u_i{}' u_j{}'}$ is the turbulence kinetic energy, and δ_{ij} is the Kronecker delta function (Lien & Yee, 2004).

Moreover, in RANS, there are two-equations models for two turbulence properties, the turbulence kinetic energy (k) and either the dissipation rate of turbulence kinetic energy (ε) or the specific dissipation rate (ω). The two models are the $k-\omega$ and $k-\varepsilon$. Both models are applicable to solve turbulent flows at high Reynolds numbers only. Still, there is a limitation which is inaccuracy to predict the flow close to walls (Yusof et al., 2020).

3.2.3. Large Eddy Simulation

LES was first proposed by Smagorinsky in 1963 for atmospheric flow simulation. Apart from the increase in computing power, the incapability of RANS in handling complex turbulent flow problems became a huge factor behind the quick development and wide range of applications of LES from the handling 1980s (Zhiyin, 2015).

One can define LES as an intermediate technique between the direct simulation of turbulent flows and the solution of the Reynolds-averaged equations. The contribution of the large, energy-carrying eddies to momentum and energy transfer is computed exactly, and only the effect of the smallest scales of turbulence is modelled (Piomelli, 1999).

This approach is based on the use of a filtering operation: a filtered (or resolved or large scale) variable, denoted by and overbar, is defined as:

$$\bar{f}(x) = \int_D f(x')G(x, x', \Delta)dx' \tag{3.15}$$

where D is the entire domain and G is the filter function. The size of the smaller resolved eddies is related to the length scale of the smoothing operator, the filter width denoted by Δ. The grid size should be sufficiently fine to allow eddies of size Δ to be represented accurately (Piomelli, 2014).

3.3. Implemented turbulence models

Two distinct turbulence modelling methods were implemented: a Reynolds-averaged simulation (RANS) and LES. For the two-dimensional approach, LES was implemented using the Smagorinsky model, and for the full three-dimensional simulation the k−ω SST model.

3.3.1. Smagorinsky SGS model

The Smagorinsky sub-grid scale (SGS) model was developed by Joseph Smagorinsky, and it is based on the eddy viscosity assumption, which requires a linear relationship between the SGS stress and the resolved rate of the strain tensor. Sub-grid scale modelling refers to the representation of important physical processes, on a small scale, that happen at length-scales that cannot be adequately solved on a computational mesh. The sub-grid scale stress tensor is:

$$\tau_{ij} = \overline{u_i u_j} - \bar{u}_i \bar{u}_j \tag{3.16}$$

$$\tau_{ij} - \frac{1}{3}\tau_{kk}\delta_{ij} = 2\nu_{sgs}\bar{S}_{ij} \tag{3.17}$$

Where

$$\bar{S}_{ij} = \frac{1}{2}\left(\frac{\partial \overline{u_i}}{\partial x_j} + \frac{\partial \overline{u_j}}{\partial x_i}\right) \tag{3.18}$$

In the Smagorinsky model, the kinematic sub-grid eddy-viscosity is assumed to be proportional to the sub-grid characteristic length scale Δ and a characteristic turbulent velocity taken as the local strain rate.

$$\nu_{sgs} = c_s \Delta \sqrt{2\bar{S}_{ij}\bar{S}_{ij}} \tag{3.19}$$

where c_s is the Smagorinsky constant and its default value is 0.094. In OpenFOAM, the method for calculating the characteristic length scale is specified in the `turbulenceProperties` dictionary and, for this work, the chosen method is cubeRootVol (Meneveau, 2010; Nicoud & Ducros, 1999; Nozaki, 2016).

3.3.2. K$-\omega$ SST model

The k$-\omega$ SST model was first proposed by Menter (1993), and it is a two-equation model where besides the Navier-Stokes equations, the turbulence kinetic energy (k) and the specific dissipation rate of turbulence kinetic energy (ω) are solved. The ω value represents the rate at which k is converted into thermal energy, per unit volume and time, as a result, it possesses the units of a frequency.

The basic idea of this model is to use a blend between k$-\varepsilon$ (far from the wall) and k$-\omega$ (close to the wall). The k$-\omega$ model shows a bigger degree of accuracy than the k$-\varepsilon$ model near-wall layers, and as a result, has been successful for flows with moderate adverse pressure gradients (Menter et al., 2003).

The value for ω at the wall boundaries is given by equation (3.20) where ν is the kinematic viscosity, $\beta_1 = 0.075$ is a constant and Δy_1 is the distance to the first cell-center (Wilcox, 1988). It is important to bear in mind that the equation is valid for $\Delta y_1 < 3$ and that the near-wall grid is further refined, thus the value tends to infinity.

$$\omega_{wall} = 10\frac{6\nu}{\beta_1(\Delta y_1)^2} \tag{3.20}$$

4. NUMERICAL METHODOLOGY

For the numerical modelling, the free and open source CFD code OpenFOAM® is used along with the post-processing and visualization software ParaView® and both are running on the OS Ubuntu 22.04 LTS. The simulations are performed on a workstation equipped with six parallel-running Intel® Core i7 CPUs clocked at 3.5 GHz.

To resolve the Navier Stokes equations, the transient solver for incompressible, turbulent flows `pimpleFoam` is used. It is important to refer that the parameter `nOuterCorrectors` (`fvSolution` dictionary), which represents how many times the system is solved, is set to 1 and, as a result, the PISO (Pressure Implicit with Splitting of Operators) algorithm is replicated. The main reason for selecting this solver is the fact that it possesses an advantageous parameter called `adjustTimeStep` that automatically adjusts the time step (Δt_s) to prevent the Courant number, equation (4.1), from being larger than 1. The reason behind this is that a Courant number of less than 1 is required to achieve temporal accuracy and numerical stability.

$$Co = \frac{\Delta t_s |U|}{\Delta x} \tag{4.1}$$

where $|U|$ is the magnitude of the velocity through the cell and Δx is the cell size in the direction of the velocity (Greenshields, 2022). During the performed simulations the maximum Courant number is kept no larger than 0.8.

The turbulence properties were calculated with a tool available in the CFD Online forum. Given the freestream velocity, the turbulence intensity (10%) and the turbulence length scale which is equal to the chord length of the panel (CFD Online, n.d.).

Residuals are the quantification of the numerical error of the solution and in OpenFOAM, the user prescribes the solver tolerance for each unknown variable, *i.e.*, a final target residual, below which the solution can be considered accurate enough and thus the solver progress for the next time step calculation. In this work, the normalized tolerance is set to 1×10^{-6} for the kinematic pressure, and 1×10^{-5} for the velocity components (U_x, U_y and U_z) and turbulence scalars.

4.1. Computational domain and meshing

4.1.1. Two-dimensional simulation

As this work represents a first learning experience using OpenFOAM, 2D simulations were performed to acquire knowledge within the simulation software. Moreover, this simplification can be particularly useful to conduct preliminary analysis and to gain confidence before progressing to more complex 3D simulations.Therefore, simulations for tilt angles of 25º, 30º and 40º were performed for a Reynolds number of 1×10^5 and with an inlet velocity profile following the power law equation – Equation (2.5). The computational domain along with the name of the boundary is shown in Figure 4.1 where *L* represents the chord length of the panel and is equal to 2 m. It is also important to refer that OpenFOAM always operates in a 3-dimensional Cartesian coordinate system and all geometries are generated in 3 dimensions. To solve in 2 dimensions, it is essential to specify a special boundary condition '`empty`' on the faces normal to the 3rd dimension for which no solution is needed. In this work, it is the z-direction (Greenshields, 2022). The boundary type for each face is summarized in Table 4.1.

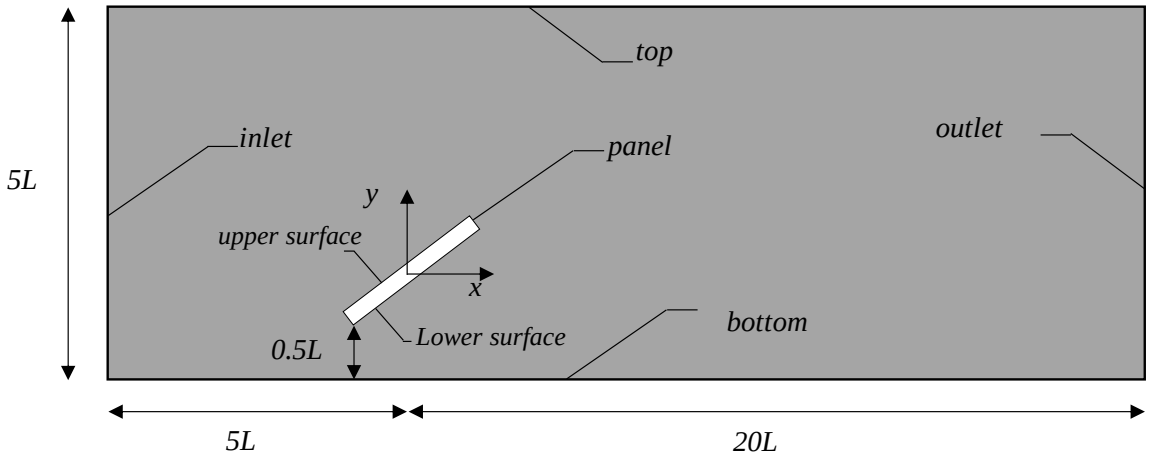

Figure 4.1. Size of the 2D computational domain and boundaries.

Table 4.1. Boundary type for the 2D computational domain.

Boundary Name	Boundary type	Details
inlet	patch	Fixed profile
outlet	patch	Fixed value
panel	wall	No slip
top	patch	Zero Gradient
bottom	wall	No slip
frontAndBack	empty	No solution required

Boundaries defined as 'patch' are a generic type of boundary condition containing no geometric or topological information about the mesh. The computational domain and the grid itself are generated with the `blockMesh` utility as it is quite a simple geometry. The principle behind this is to decompose the domain geometry of three-dimensional, hexahedral blocks. Each block is defined by 8 vertices and one can specify the number of cells in each direction of the block (Greenshields, 2022).

Given that CFD obtains an approximate solution based on discrete grids, the accuracy of the approximate solution depends on the grid quality. The grid independence test is a process used to find the optimal grid condition that has the smallest number of grids without generating a difference in the numerical results based on the evaluation of various grid conditions (Lee et al., 2020). The total number of cells is about 816×10^3 and is chosen based on a grid independence test among three different grids having 402×10^3 (G1); 816×10^3 (G2); and $1{,}171 \times 10^3$ (G3) cells. The test is performed based on the mean pressure coefficient (C_p) in the upper surface of the panel for a 0º wind direction, 30º tilt angle and the refinement ratio is 1.2 for the x and y directions.

Table 4.2 gathers the number of cells and the respective execution time (Δt_{exec}), in hours, for a 20 second flow simulation with the three different grid approaches tested in this chapter.

Table 4.2. Grid Independence test properties

Grid	Number of cells	Δt_{exec} [h]
Coarse (G1)	402×10^3	6.1
Medium (G2)	816×10^3	13.5
Fine (G3)	$1{,}171 \times 10^3$	20.1

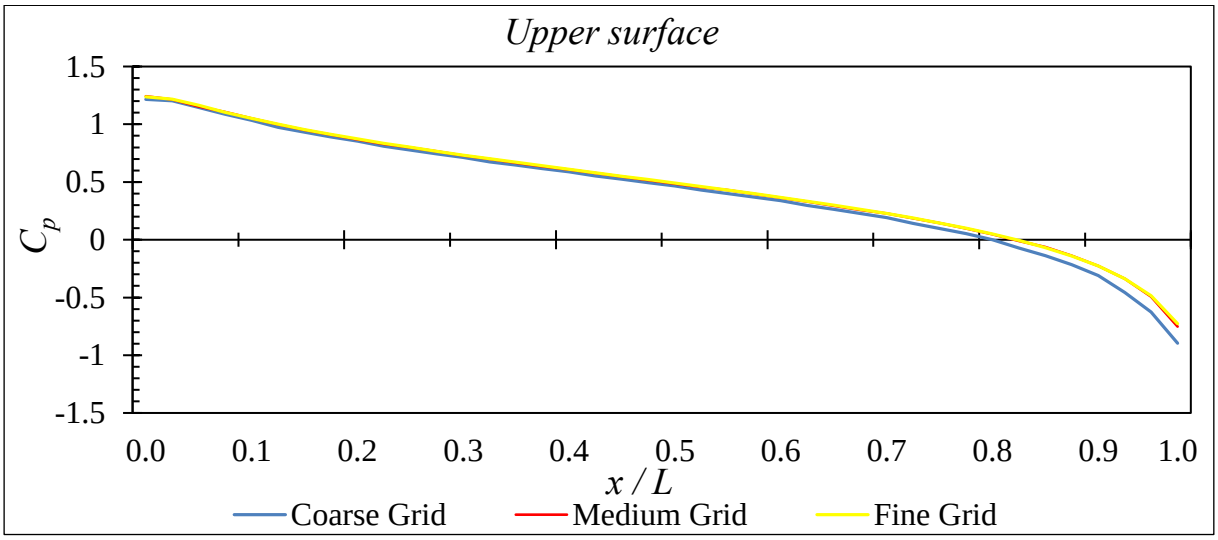

Figure 4.2. Comparison between the mean pressure coefficient in the upper surface of the panel for the three different grids.

40 probes, equally spaced, were located along the chord length of the panel and the results were saved with a frequency of 100 Hz. Figure 4.2 shows the time average values for the pressure coefficient (C_p) for the three different grids used in the test. The difference between the globally averaged values for G1 and G2 is about 9.1% and between G2 and G3 0.63%, thus the grid selected for the simulations is grid G2.

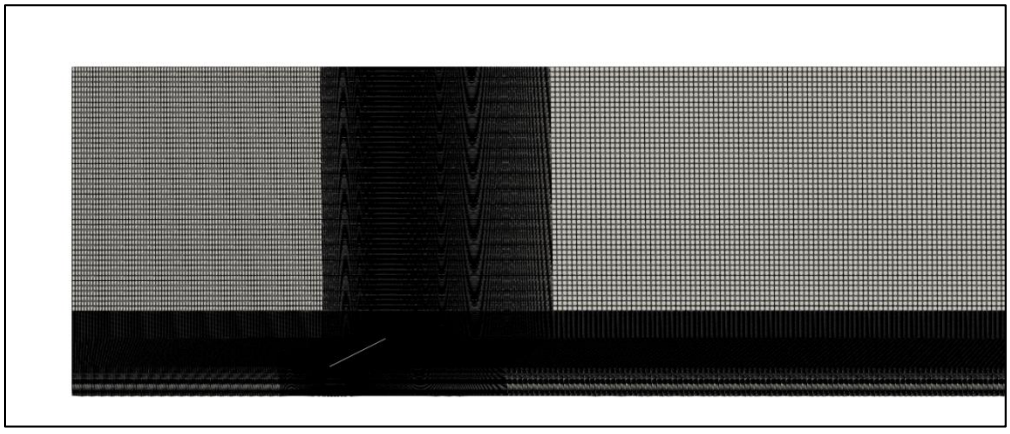

Figure 4.3. Grid G2 used to perform the simulations.

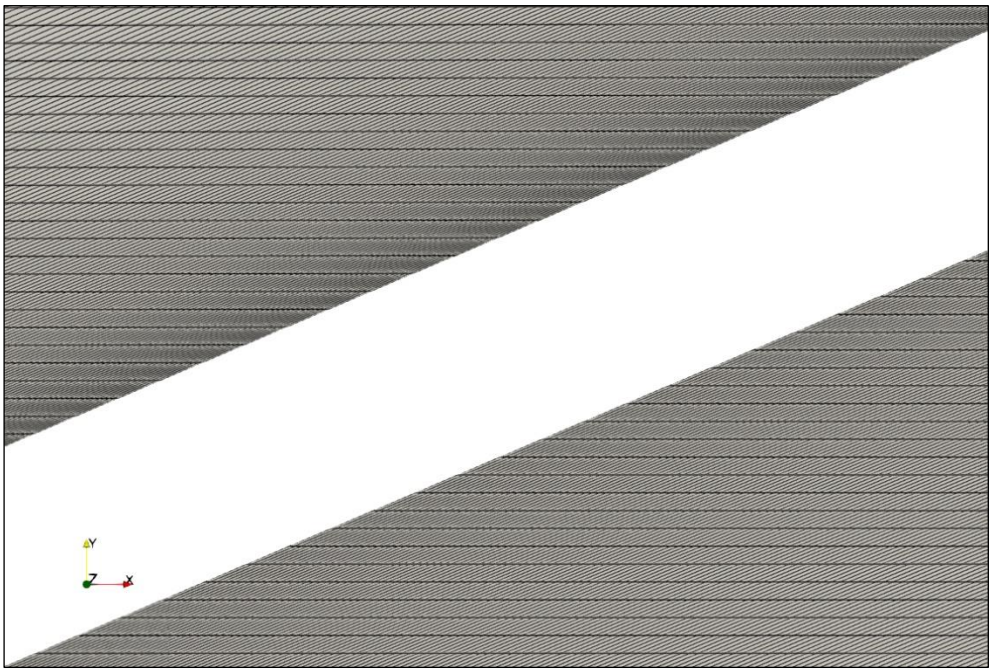

Figure 4.4. Near wall medium grid detail.

The mean y^+ value (*i.e.*, dimensionless distance from the wall to the first grid point) is about 0.87 for the duration of the simulation.

To ensure grid quality, it is important to verify the validity of a mesh. This is done with the `checkMesh` utility that generates a report with all the important properties such as aspect ratio, mesh non-orthogonality and skewness. In Figure 4.5 the output generated by the aforementioned utility is shown and demonstrates that all the important parameters to validate the mesh are met.

```
Checking geometry...
    Overall domain bounding box (-10 -1.51732 0) (40 10 0.1)
    Mesh has 2 geometric (non-empty/wedge) directions (1 1 0)
    Mesh has 2 solution (non-empty) directions (1 1 0)
    All edges aligned with or perpendicular to non-empty directions.
    Boundary openness (-3.44372e-18 -2.21312e-17 4.08334e-14) OK.
    Max cell openness = 9.91192e-16 OK.
    Max aspect ratio = 238.129 OK.
    Minimum face area = 1.17234e-06. Maximum face area = 0.030859.  Face area magnitudes OK.
    Min volume = 1.17234e-07. Max volume = 0.0030859.  Total volume = 57.5777.  Cell volumes OK.
    Mesh non-orthogonality Max: 63.5442 average: 36.8154
    Non-orthogonality check OK.
    Face pyramids OK.
    Max skewness = 1.85211 OK.
    Coupled point location match (average 0) OK.

Mesh OK.

End
```

Figure 4.5. CheckMesh output for the medium 2D grid.

4.1.2. Three-dimensional simulation

Since turbulence is always three-dimensional and after familiarizing with the software and gaining some experience, it is time to carry out 3D simulations. This will allow

for the study of how the flow varies along the span of the panel and its edges in a more complex way. However, this approach presents new challenges, as the generation of the computational domain, geometry and mesh will require different tools.

Similar to the two-dimensional simulations, the three-dimensional computational domain, as well as the nomenclature for the boundaries is shown in Figure 4.6. The Reynolds number, the PV panel tilt angles, the chord length, and the inlet velocity profile are the same as the ones used for the two-dimensional approach. In addition, simulations for a wind direction of 30º and 180º (See Figure 4.7) were performed for a 25º tilt angle in which the wind approaches from the left.

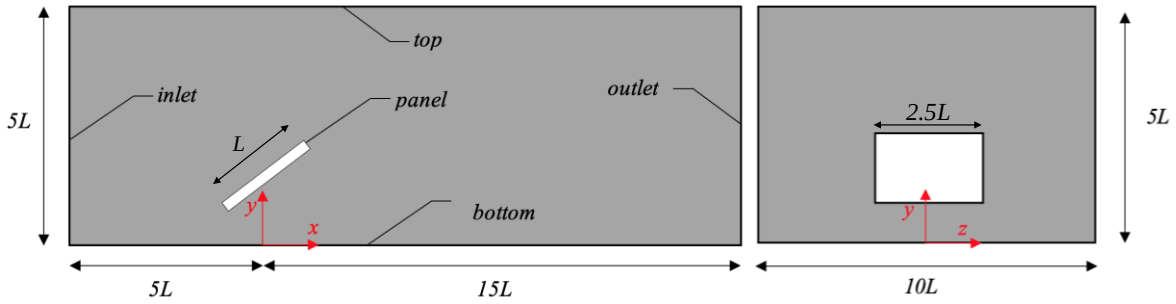

Figure 4.6. Size of the 3D computational domain and boundaries.

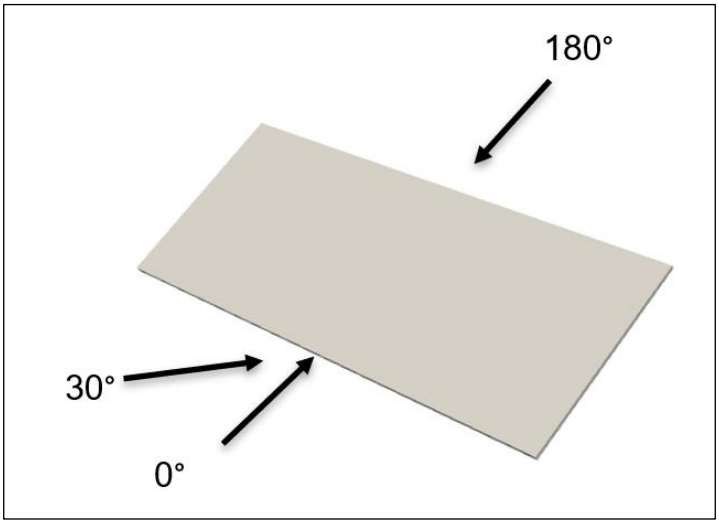

Figure 4.7. Representation of the three different wind direction (θ) on the panel.

Table 4.3. Boundary type for the 3D computational domain.

Boundary Name	Boundary type	Details
inlet	patch	Fixed profile
outlet	patch	Fixed value
panel	wall	No slip
top	patch	Zero Gradient
bottom	wall	No slip
frontAndBack	patch	Zero Gradient

For the grid discretization, the PV panel's 3D geometry (2 m × 5 m) with a 40 mm thickness is modelled in the commercial CAD software *Autodesk Inventor Professional 2024* and exported in stereolithography (STL) format. The computational domain, and grid, are generated with the `snappyHexMesh` utility. This powerful tool generates three-dimensional meshes containing hexahedra and split-hexahedra automatically from triangulated surface geometries, or tri-surfaces in STL or Wavefront Object (OBJ) format. This mesh-generating tool iteratively conforms the finite volumes to the surface, refining a background hex mesh that can be generated with the `blockMesh` utility. This utility also has an optional phase that allows inserting cell layers in the boundaries defined as walls (Greenshields, 2022). For the three different tilt angles, the blockage ratios in the computational domain are 2.11, 2.5 and 3.21%, respectively.

The generation of a good grid is crucial to guarantee that the simulation results are reliable and accurate. Hence, the cells should have restricted non-orthogonality, aspect ratios and skewness, as well as favourable element distribution and density. To achieve this, the `snappyHexMesh` tool needs high-quality tri-surfaces to start with (Brito, 2019).

To meet the mesh quality standards, refining the rough CAD exported STL file and verifying the geometry is watertight (*i.e.* completely closed) is needed. To achieve both requirements, the quality of the STL is improved with the open-source software *SALOME 9.9.0*. The highly equilateral and triangulated PV panel is shown in Figure 4.8.

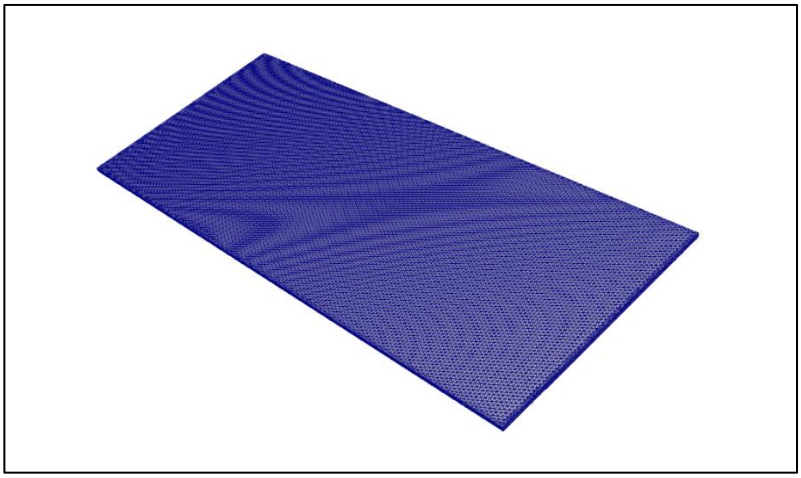

Figure 4.8. Highly triangulated and watertight STL used in the mesh generation.

Considering the available computational resources, a grid independence test was impracticable as both greater and lower levels of grid refinements resulted in grids that do not meet the quality requirements. In addition, the three different tilt angles require a different STL file which results in a different number of cells for each grid even with the same parameters in the `snappyHexMesh` dictionary. In fact, generating an acceptable grid was a huge challenge as a large number of parameters needed to be modified. Visual details about the 3D mesh generated are shown in Figure 4.9 and Figure 4.10.

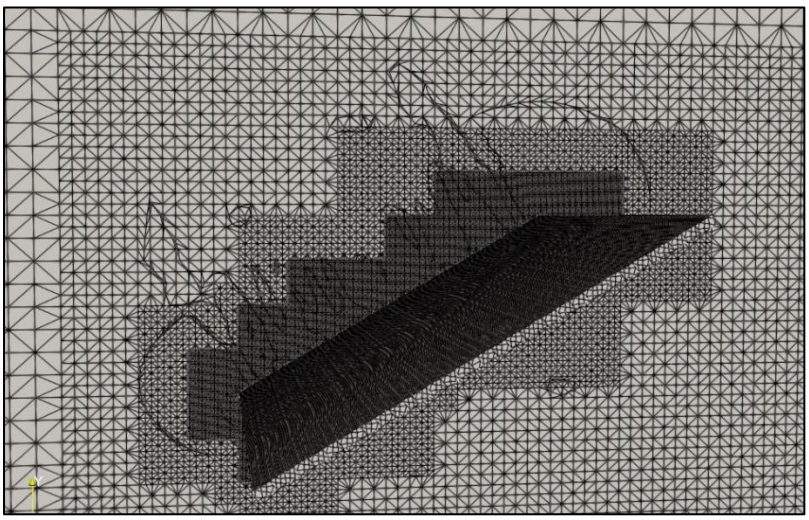

Figure 4.9. Grid generated by the `SnappyHexMesh` utility around the STL file.

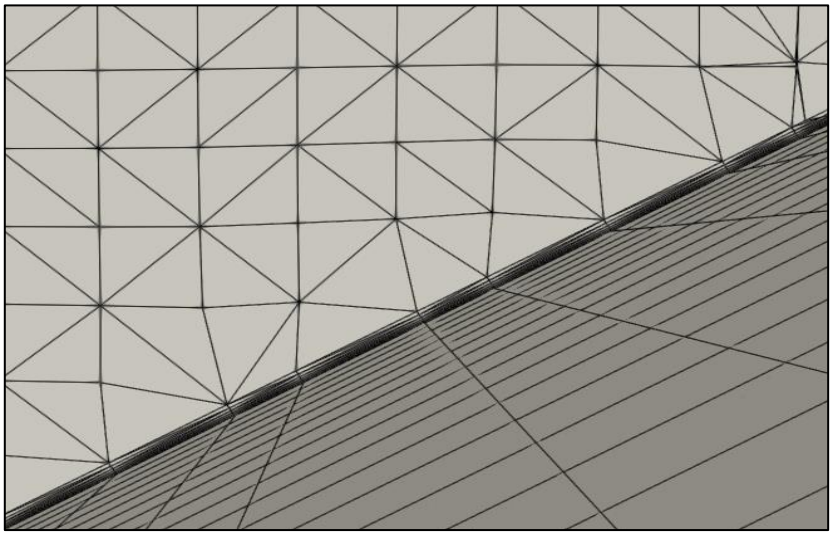

Figure 4.10. Layers inserted near the wall boundaries.

4.2. Initial and boundary conditions

Regarding the figures that represent both the two-dimensional and three-dimensional computational domains, at the `inlet` patch a velocity profile following equation (2.5) is implemented, using $\alpha = 1/7$ and $\delta = 2.5L$. To apply this varying variable, a comma-separated file (.csv) was needed. Concerning the turbulence kinetic energy (k) and the specific dissipation rate (ω) both are defined as `fixedValue` type and calculated with the tool specified at the beginning of the current chapter. With respect to the eddy-viscosity (`nut`), it is automatically computed throughout the domain.

For the `outlet` patch, fully developed conditions are assumed for the velocity and turbulent scalars except for the kinematic pressure (p), which is set as a fixed zero value. This is a common practice in OpenFOAM simulations, so the pressure field within the domain is relative (Greenshields, 2022).

On solid surfaces, treated as wall-type patches, the no-slip condition is imposed for the velocity field, hence (k) tends to zero. For the eddy-viscosity (`nut`) and the specific dissipation rate (ω) wall functions `nutSpaldingWallFunction` and `omegaWallFunction` are implemented as $y^+ \approx 1$. For the two-dimensional approach, the front and back domain boundaries the `empty` boundary condition is implemented to guarantee a 2D domain whereas, in the three-dimensional domain, the `front`, `back` and `top` are defined as `patch` boundaries.

The respective dictionaries with the initial values for the boundary conditions are shown in Appendix A – Boundary Conditions Dictionaries

5. RESULTS AND DISCUSSION

In this chapter, the numerical prediction of the wind loads on PV panels is exhibited and compared with the wind-tunnel measurements performed by (Abiola-Ogedengbe et al., (2015). The simulations are run for a total of 20 seconds of flow time and the average of the last 15 seconds is taken to analyze results.

Mean C_p values are along the mid-lane of the PV panel on both upper and lower surface for wind directions θ of 0º and 180º, and tilt angles of 25º, 30º and 40º are compared with experimental data available in the literature. It is important to consider that the experimental full-scale dimension is different and the CFD model does not possess the structural components at the back of the panel. To obtain the values, 40 evenly spaced probes, located along the mid-lane of the geometry, wrote the values of the kinematic pressure p_k [m^2/s^2] every 0.01 seconds. Afterwards, the values were converted to represent the dimensionless parameter C_p with equation (5.1)

$$C_p = \left(2 \times \frac{1}{{U_0}^2}\right) \times p_k \tag{5.1}$$

5.1. Two-dimensional Smagorinsky model results

The simulated, time-averaged, C_p distribution in both the upper (sun-facing) and lower (ground-facing) surfaces of the PV panel, 40 evenly spaced probes for the three different tilt angles are shown in the following figures:

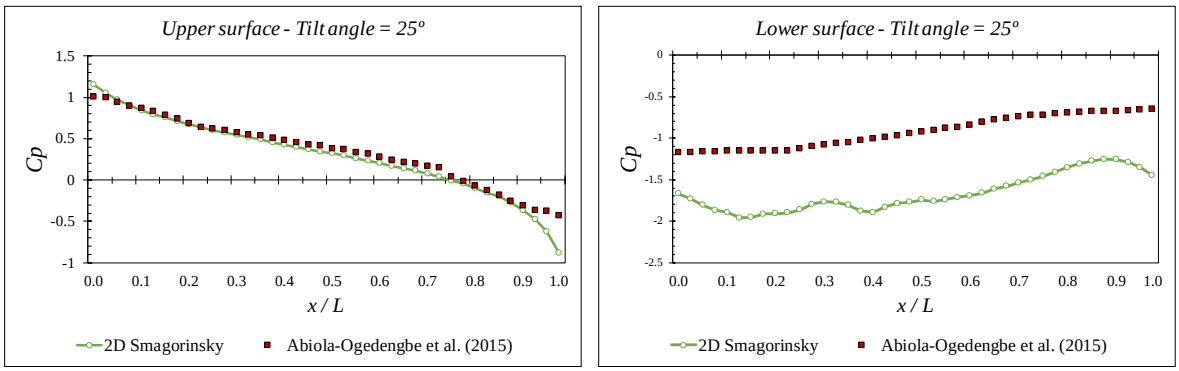

(a) (b)

Figure 5.1. Mean C_p distribution on both upper (a) and lower (b) surfaces for a tilt angle of 25º. 2D LES employing the Smagorinsky turbulence model.

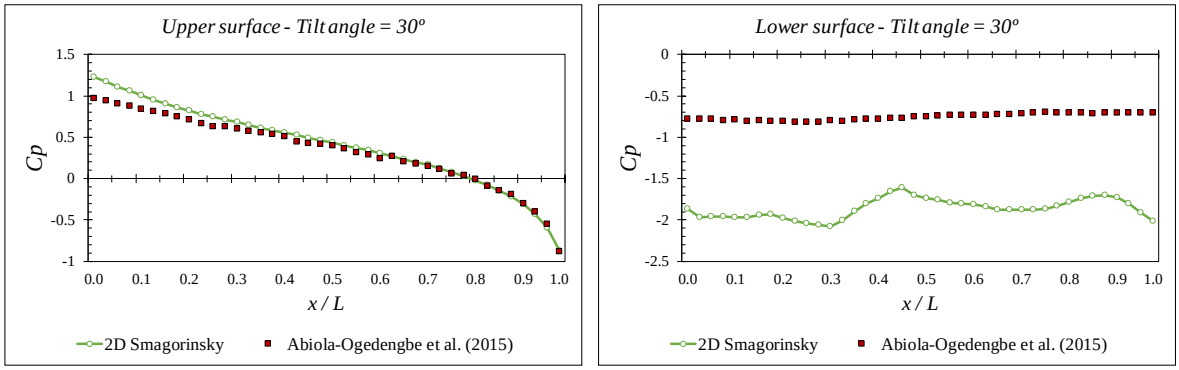

(a) (b)

Figure 5.2. Mean C_p distribution on both upper (a) and lower (b) surfaces for a tilt angle of 30º. 2D LES employing the Smagorinsky turbulence model.

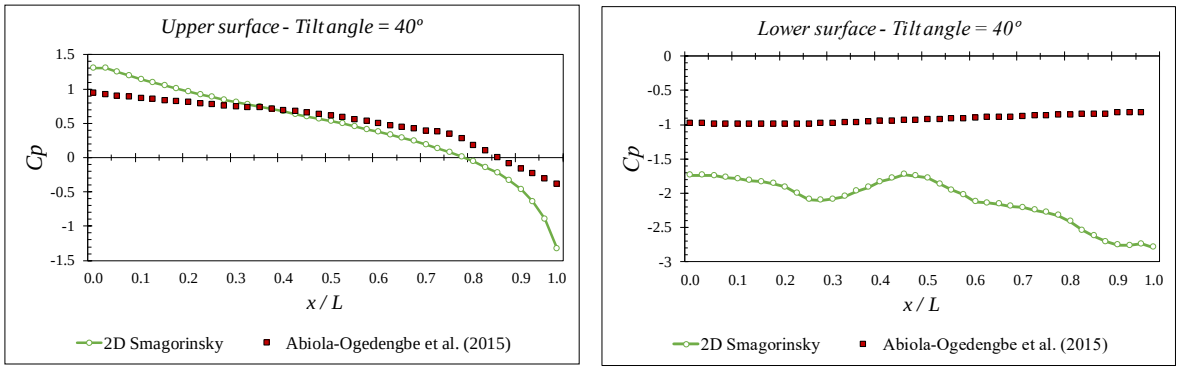

(a) (b)

Figure 5.3. Mean C_p distribution on both upper (a) and lower (b) surfaces for a tilt angle of 40º. 2D LES employing the Smagorinsky turbulence model.

In general, the mid-lane C_p distribution on the front surface shows that it decreases from the highest positive value at the leading edge to the lowest negative value at the trailing edge where the flow detaches from the upper surface. Thus, on the front surface, maximum wind loads occur at the leading edge of the panel. Furthermore, C_p magnitudes are found to be higher for larger tilt angles.

For a tilt angle of 25º, despite some small divergences near the leading edge and the trailing edge of the PV panel, the computational prediction agrees with the experimental data. For a tilt angle of 30º, there is a small divergence on the leading edge and a generally good agreement towards the trailing edge between both numerical and experimental values. The numerical result for a 40º tilt angle is the one that shows a bigger discrepancy when compared to the experimental data, overestimating the values on both the leading and trailing edges. As a result, it can be concluded that the numerical prediction follows the trend acceptably.

Considering the lower surface of the PV panel, the numerical predictions underestimate the values for the three different tilt angles and show a more irregular trend along the chord length comparatively to the experimental data. One possible justification for this disagreement between the two sets is the ground clearance which is not stated in (Abiola-Ogedengbe et al., 2015), being about 1 m in the CFD model.

Figure 5.4 shows vortex shedding from the trailing edge where the flow accelerates. This detailed view showing the appearance of eddies, which is not visible when performing RANS, is characteristic of LES.

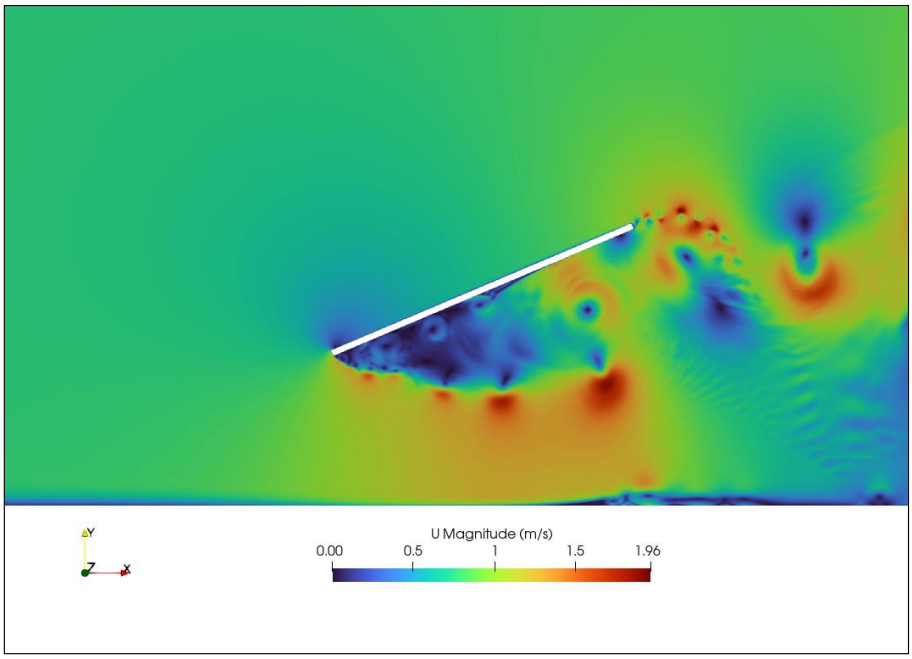

Figure 5.4. Velocity magnitude contour at t = 13 s (25º tilt angle). LES

The Strouhal number, equation (5.2), that is, the dimensionless shedding frequency of the vortices behind the flat plate was calculated and then compared with the experimental result from (Chen & Fang, 1996). It is obtained by calculating the highest frequency for the lift coefficient through the calculation of the Fourier transform.

$$St = \frac{fL}{U} \tag{5.2}$$

where U is the velocity, f the frequency and L the characteristic length which in this case is the chord length of the panel. For the Fourier analysis in *Microsoft Excel*, the input sample has to be 2^n sized, where n is an integer number. In this case, an input of 2048 values was

used. The vortex shedding frequency is plotted in Figure 5.5, and the *St* corresponds to the highest amplitude.

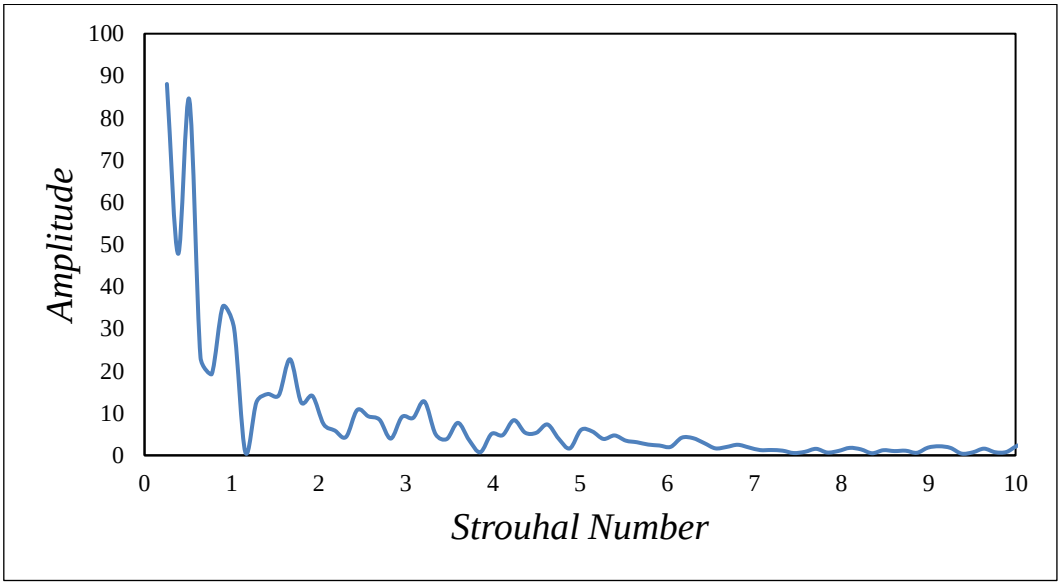

Figure 5.5. Lift coefficient as a function of the Strouhal number for a 30º tilt angle.

The obtained Strouhal number for a 30º tilt angle is equal to 0.26, whereas the experimental value in (Chen & Fang, 1996) is of 0.31. There is a difference of about 16.2% that can be justified by the existence of beveled sharp edges on the flat plates used for the experimental study.

5.2. Three-dimensional k−ω SST model results

Similar to the two-dimensional approach, time-averaged C_p distribution in both the upper and lower surfaces of the PV panel are shown in the following figures and compared with experimental data. Similar conclusions can be made between the current approach and the two-dimensional one; C_p has a maximum value at the leading edge and decreases to a negative value towards the trailing edge and it increases with the tilt angle.

Considering the upper surface there is a consistency between the numerical prediction and the experimental data and a better agreement for the lower surface when compared with the two-dimensional approach.

For the three different inclinations, the tilt angle of 40º is the one that shows a better agreement between numerical and experimental values, showing a small divergence on the trailing edge. The other tilt angles studied show greater differences on both the leading and

trailing edges. Regarding the lower surface, this three-dimensional approach follows the experimental trend in a closer way when compared with the 2D LES study. However, some disparities are found.

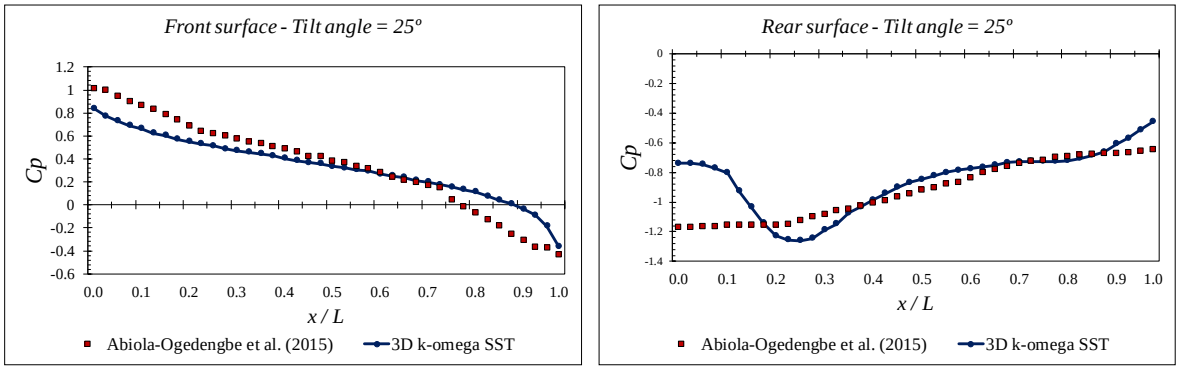

(a) (b)

Figure 5.6. Mean C_p distribution on both front (a) and rear (b) surfaces for a tilt angle of 25º.

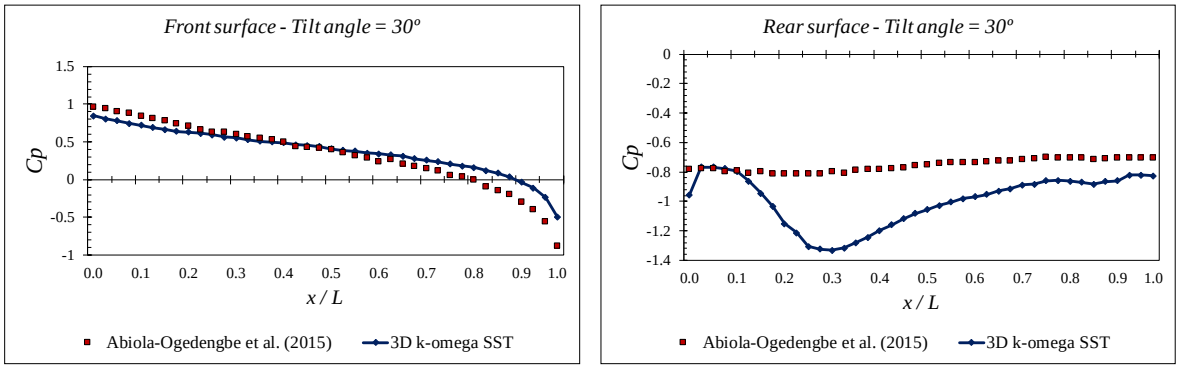

(a) (b)

Figure 5.7. Mean C_p distribution on both front (a) and rear (b) surfaces for a tilt angle of 30º.

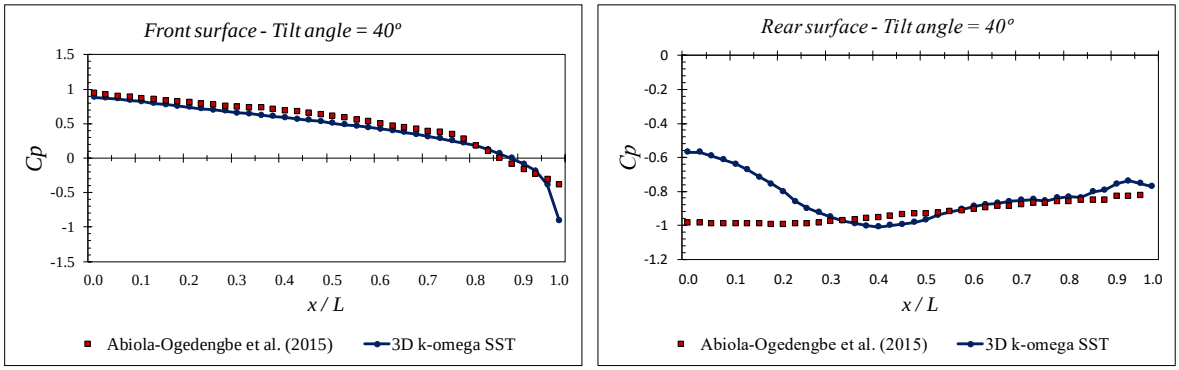

(a) (b)

Figure 5.8. Mean C_p distribution on both front (a) and rear (b) surfaces for a tilt angle of 40º.

As this second approach truly demonstrates the three-dimensional nature of the flow around PV panels, in Figure 5.9 and Figure 5.10 it can be observed that the pressure

distribution is symmetrical about the mid-lane of the panel in both upper and lower surfaces. For the front surface (windward surface as the wind direction is 0º), the kinematic pressure values and, consequently, the C_p is higher on the middle of the panel and then decrease towards the side edges. This occurrence is witnessed as the flow accelerates towards the edges and creates a low-pressure region on the panel surface (Jubayer & Hengan, 2015).

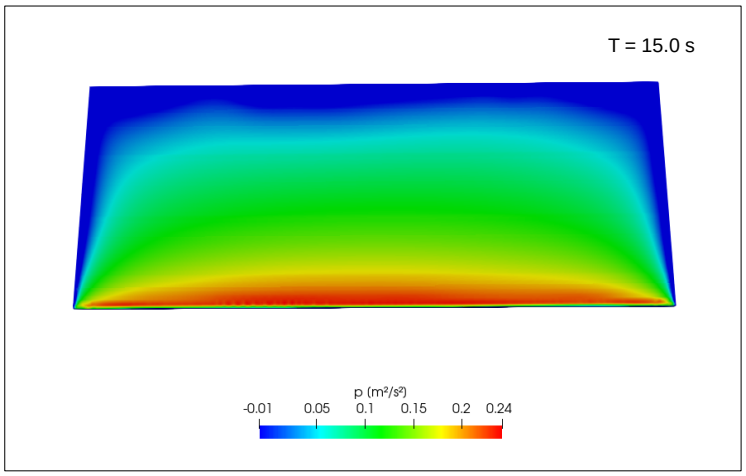

Figure 5.9. Kinematic pressure distribution on the upper surface of the PV panel at t = 15 s (25º tilt angle).

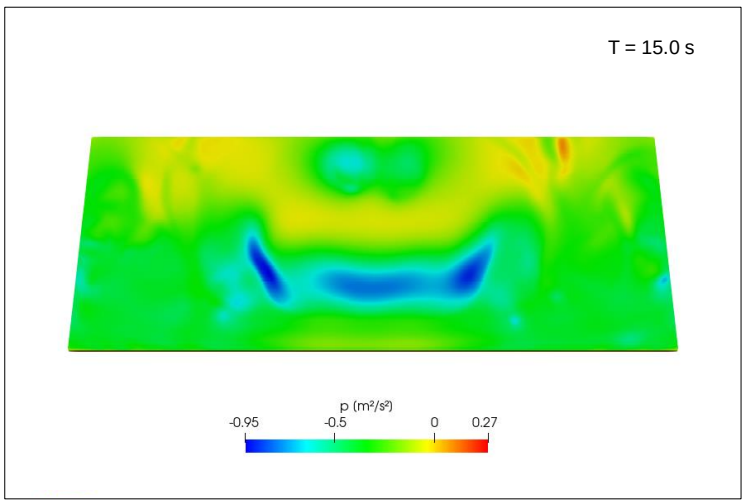

Figure 5.10. Kinematic pressure distribution on the lower surface of the PV panel at t = 15 s (25º tilt angle).

Regarding the aerodynamic loading analysis, similar to the pressure coefficient, the gathering process involving the mean values for the drag and lift coefficients was also performed only for the last 15 seconds of the simulation time.

Figure 5.11 shows that the drag coefficient increases with the tilt angle to a maximum value of 1.65 at 40º, having a greater raise between 25º and 30º (about 18%) and a less steep

one between 30 and 40º (about 1.44%). This is expected as a higher tilt angle means a bigger reference area that is in contact with the flow.

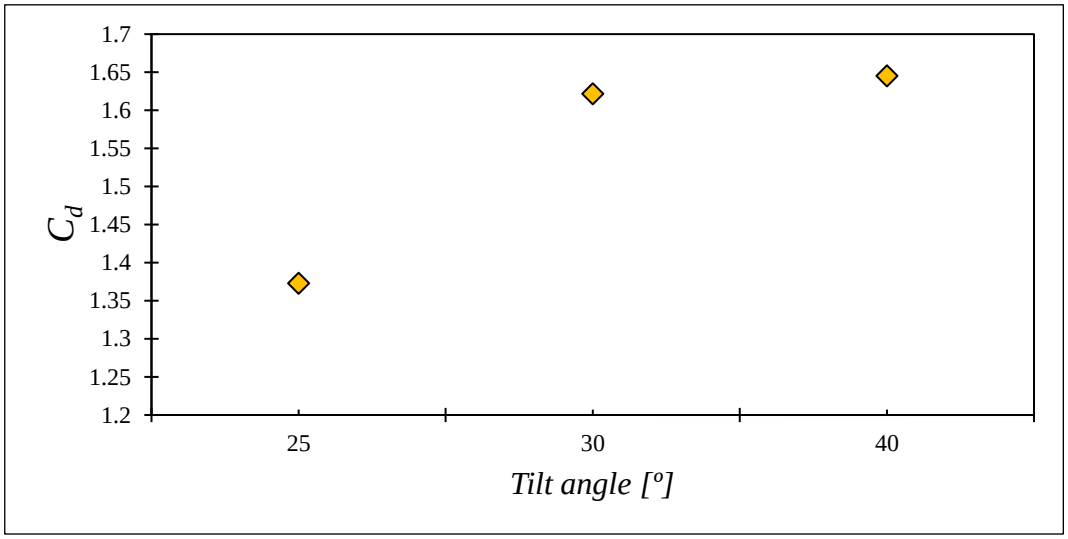

Figure 5.11. Computed Drag coefficient for the three different tilt angles studied in this work.

In this current scenario, the wind direction is 0º and, as a result, a negative lift is generated. Its modulus decreases with higher values of tilt angle to a value of -1.96 as presented in Figure 5.12. It can be observed that the values between the 25º and 30º exhibit a subtle difference (2.46%), whereas the 40º tilt angle is the one that shows a bigger variation (about 30%) with a lower modulus, between the three tilt angles studied, for this coefficient.

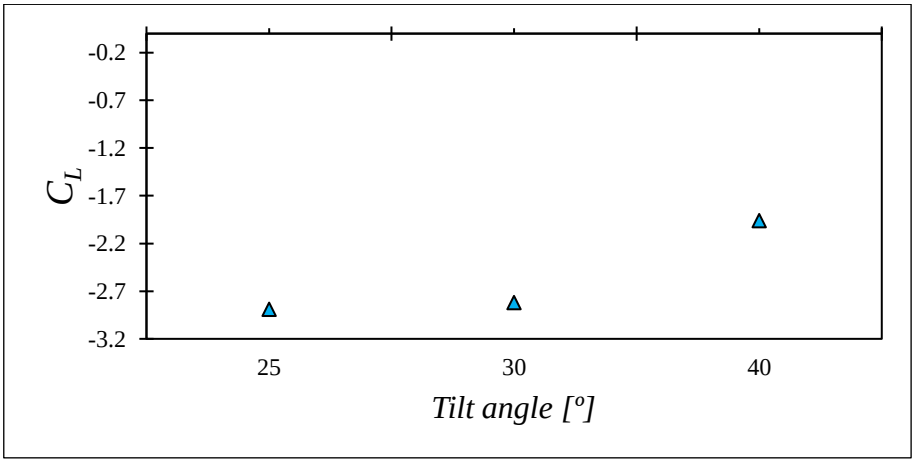

Figure 5.12. Computed Lift coefficient for the three different tilt angles studied in this work.

Figure 5.13 shows the velocity contour for one of the RANS simulations. As mentioned before, it is clear that the eddies are not so visible when compared with LES predictions.

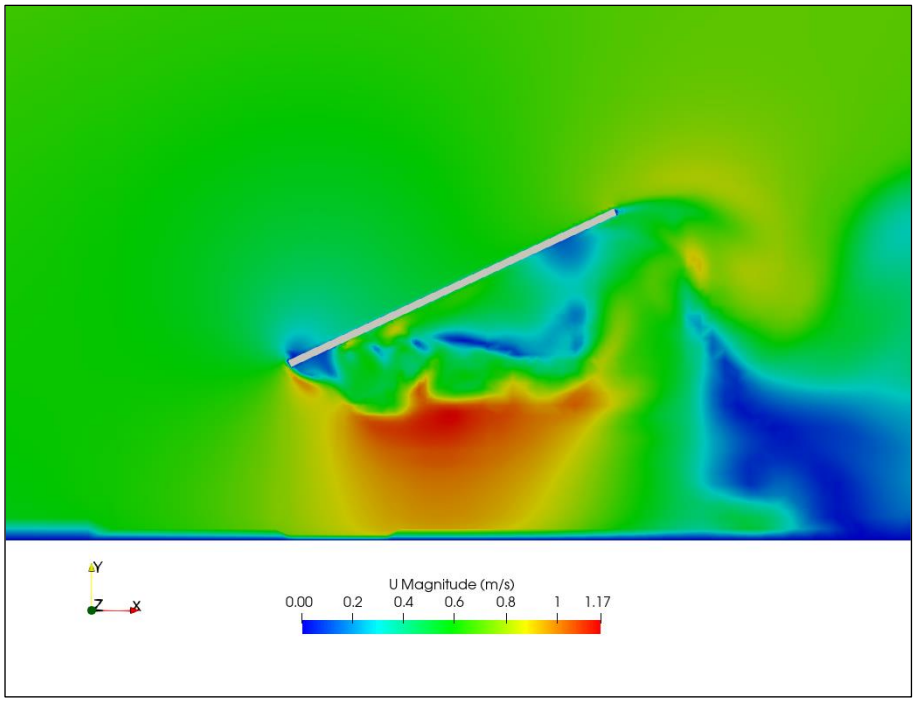

Figure 5.13. Velocity magnitude contour at t = 13 s (25º tilt angle). RANS

The resultant pressure coefficient is the difference between the pressure coefficient values on the upper (u) surface and lower (l) surface of the panel. The values were only calculated for $\theta = 0º$.

$$\Delta C_p = C_{p_u} - C_{p_l} \tag{5.3}$$

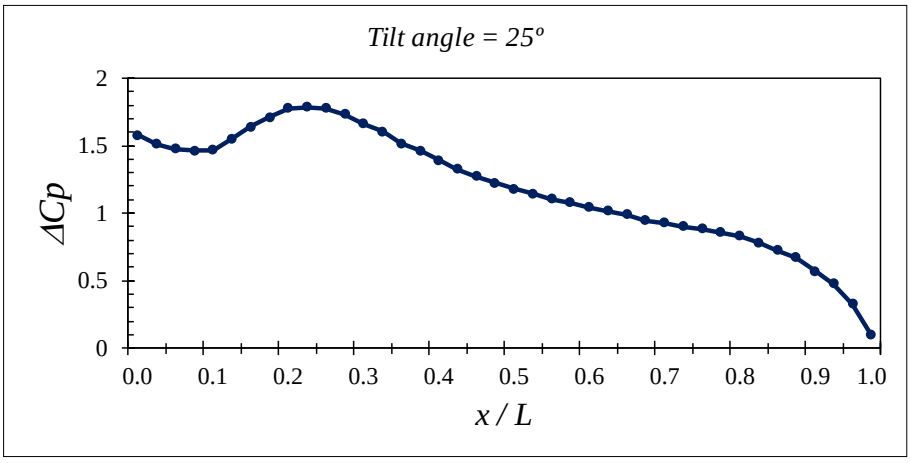

Figure 5.14. Distribution of the resultant pressure coefficient for a tilt angle of 25º.

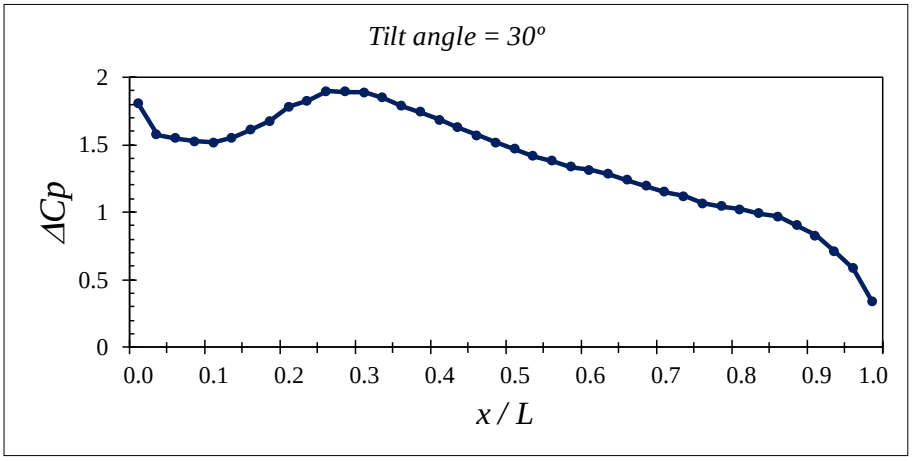

Figure 5.15. Distribution of the resultant pressure coefficient for a tilt angle of 30º.

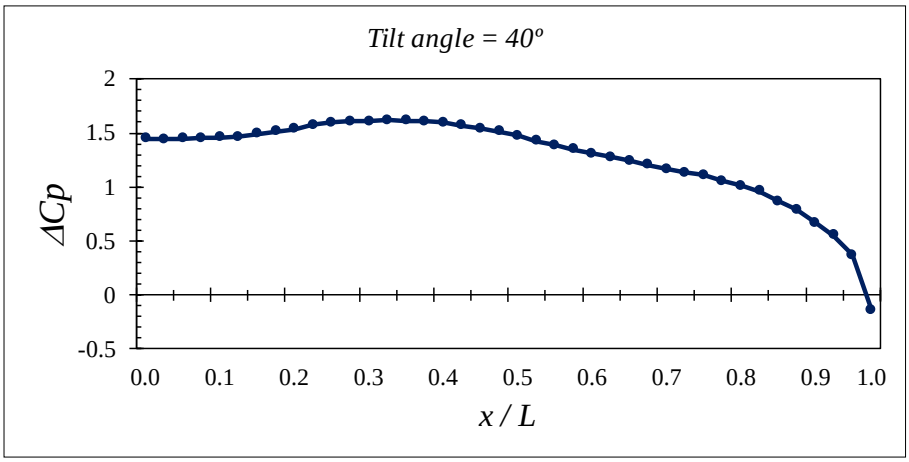

Figure 5.16. Distribution of the resultant pressure coefficient for a tilt angle of 40º.

It is shown by the previous figures that the resultant pressure coefficient decreases from the leading edge towards the trailing edge and that the higher the tilt angles the greater the pressure coefficient values, with the maximum value registered at about $x/L = 0.3$. It was also noted that the resultant is negative close to the trailing edge for the higher tilt angle analyzed in this study.

The C_p distribution for a wind direction of 180º and 25º tilt angle is shown in Figure 5.17. It should be pointed out that in this configuration, there is suction (due to the flow recirculation) at the upper surface contrary to what occurs for a wind direction of 0º. It is important to also clarify that $x/L = 1$ represents the leading edge and $x/L = 0$ the trailing edge, contrary to what happens for the figures representing the 0º wind direction. Furthermore, the numerical prediction does not match the experimental data with the same

level of accuracy when compared with the configuration exhibited at the beginning of this subchapter ($\theta = 0º$). It was also noted that the pressure distribution on both the front and rear surfaces of the PV panel is approximately symmetrical (Figure 5.18 and Figure 5.19).

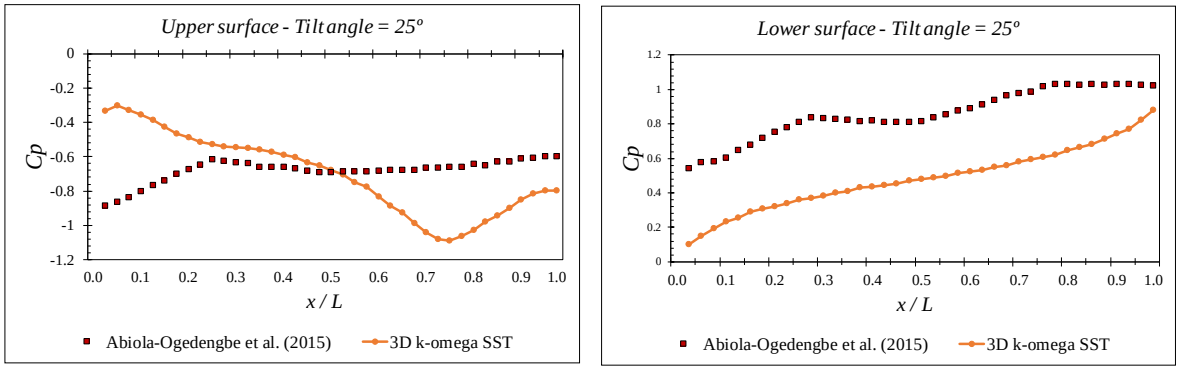

(a) (b)

Figure 5.17. Mean C_p distribution on both upper (a) and lower (b) surfaces for a tilt angle of 25º and 180º wind direction.

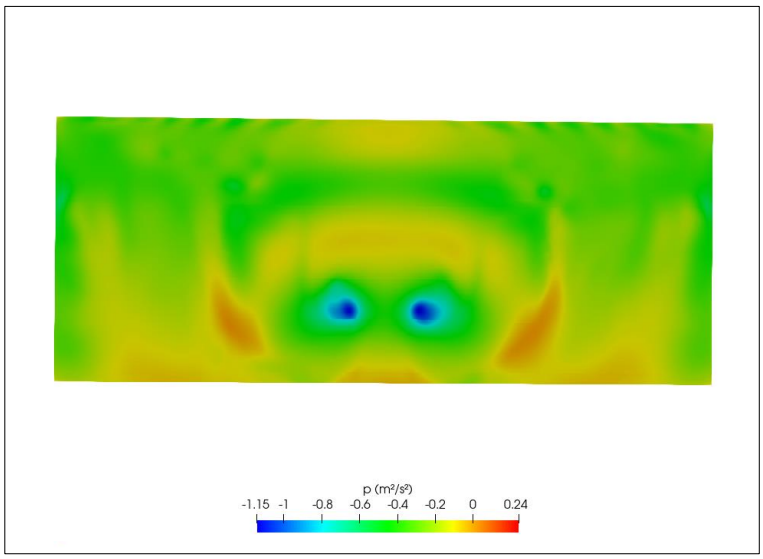

Figure 5.18. Kinematic pressure distribution on the upper surface of the PV panel with $\theta = 180º$ (25º tilt angle).

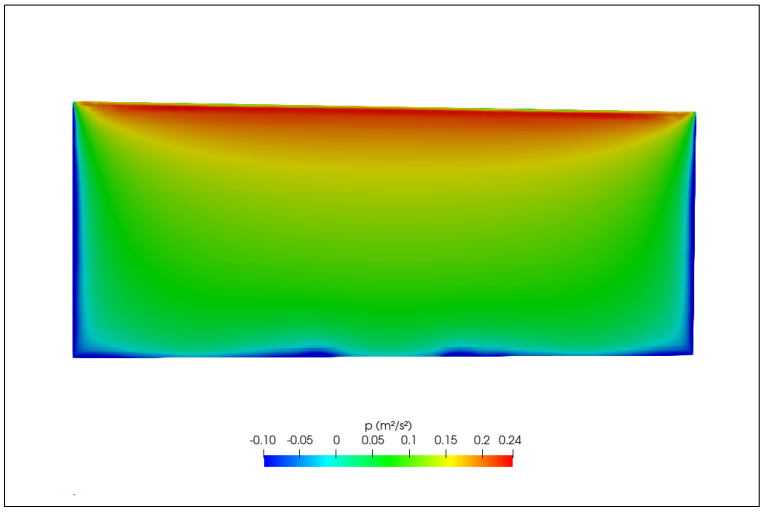

Figure 5.19. Kinematic pressure distribution on the lower surface of the PV panel with $\theta = 180^{o}$ (25^{o} tilt angle).

For the simulation with $\theta = 30^{o}$, two groups of 40 evenly spaced probes were used. However, they were not located along the mid-lane of the panel as shown for $\theta = 0^{o}$ and $\theta = 180^{o}$ (see Figure 5.20).

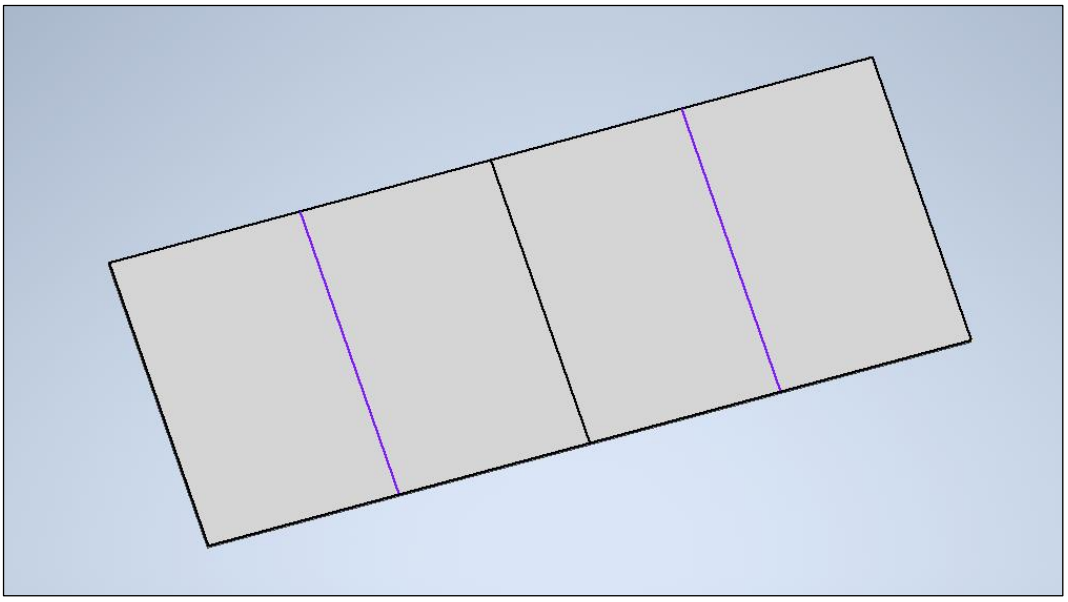

Figure 5.20. Lines (blue) where 40 evenly spaced probes were located for $\theta = 30^{o}$.

The C_p distribution on both right and left halves of the panel is shown in the following figures:

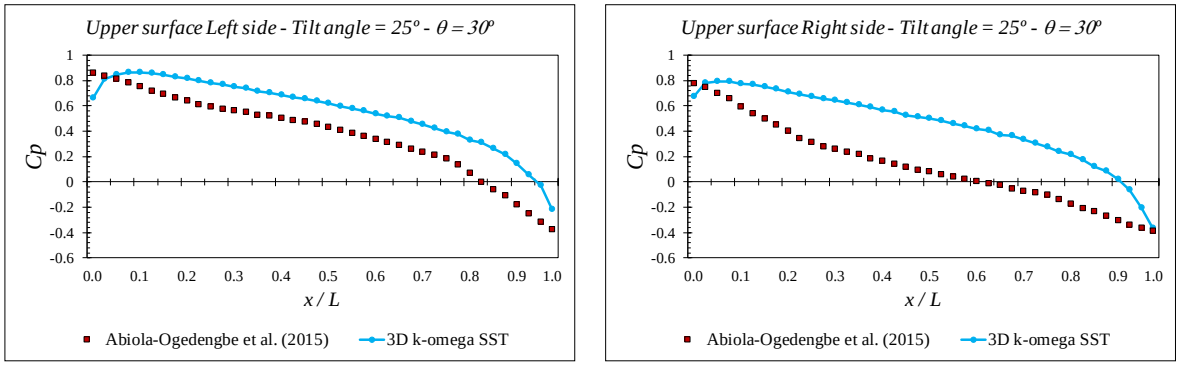

(a) (b)

Figure 5.21. Mean C_p distribution on the upper surface left (a) and right (b) halves for a tilt angle of 25º and 30º wind direction.

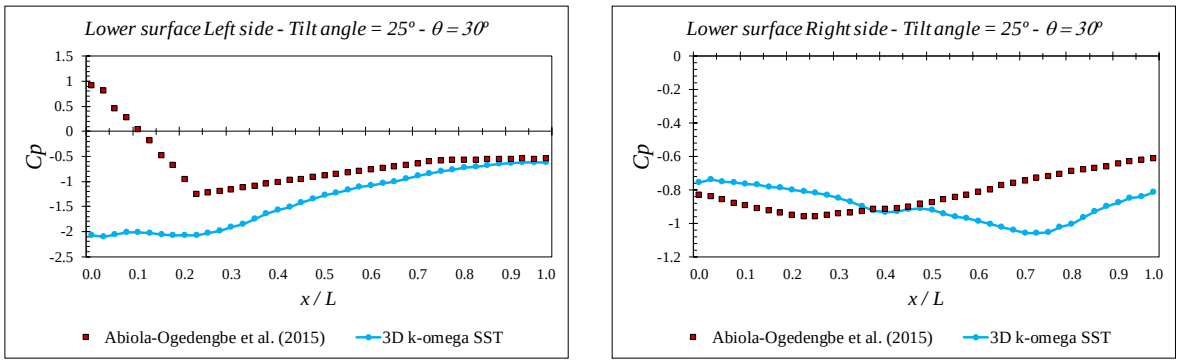

(a) (b)

Figure 5.22. Mean C_p distribution on the lower surface left (a) and right (b) halves for a tilt angle of 25º and 30º wind direction.

Regarding the upper surface, even though it overestimates the values, the numerical prediction follows the trend shown by the experimental data, having higher values close to the leading edge and decreasing towards the trailing edge.

On the other hand, the prediction on the lower surface shows bigger discrepancies. On the left side, there is a huge difference at $x/L \in [0, 0.2]$ and a minimal disagreement towards $x/L \rightarrow 1$. Moreover, regarding the right side there is better agreement between the numerical prediction and experimental data as both show negative values.

It was observed that the pressure distribution is no longer symmetrical on both the upper and lower surface of the panel having the highest positive values on the edge that first encounters the flow and the maximum negative values on the opposite edge. Figure 5.23 shows that the area in which the maximum pressure values are found is larger than the one for $\theta = 0$º and the maximum value is slightly greater. On the lower surface (Figure 5.24), there is positive pressure at a small zone on the upper center of the panel and the rest of the

distribution shows negative values with greater values at the same zone where higher positive values exist on the contrary surface.

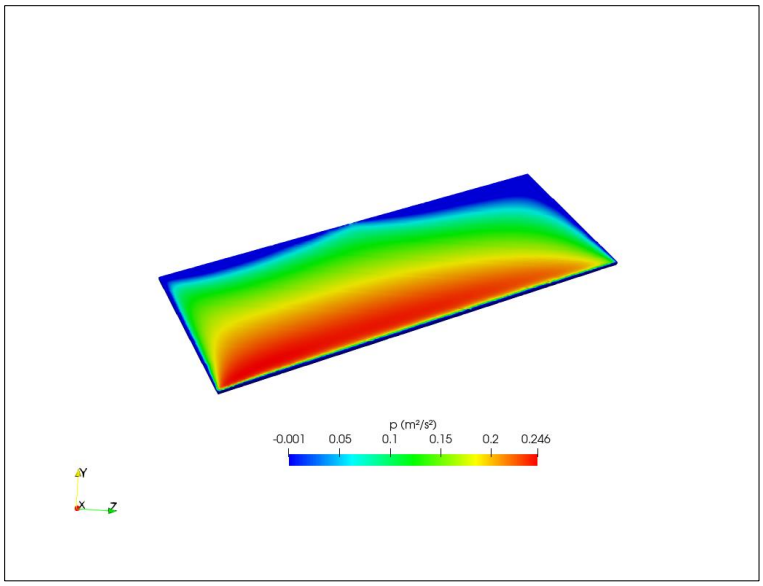

Figure 5.23. Kinematic pressure distribution on the upper surface of the PV panel with $\theta = 30^{o}$ (25^{o} tilt angle).

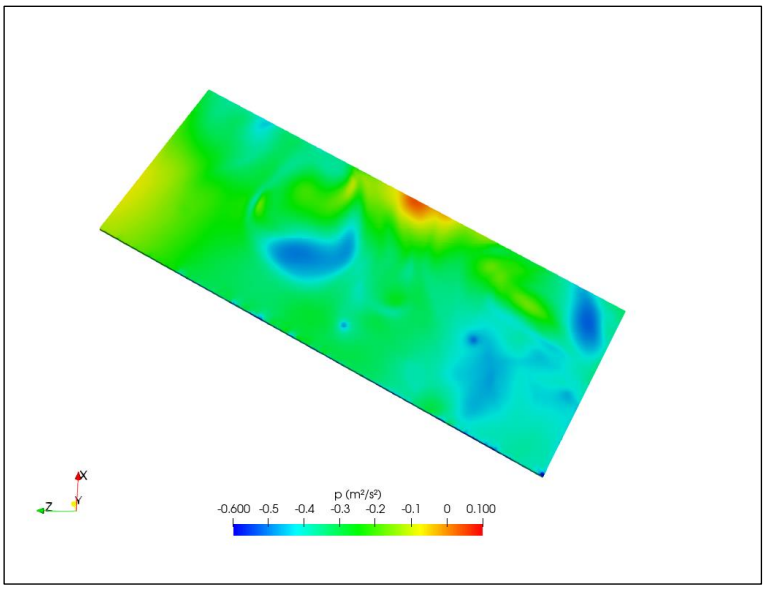

Figure 5.24. Kinematic pressure distribution on the lower surface of the PV panel with $\theta = 30^{o}$ (25^{o} tilt angle).

For more images regarding the flow streamlines for the three different tilt angles studied in this work and both wind directions, it is suggested to the reader to see Appendix B – 3D Flow Streamlines

6. CONCLUSIONS

This work presents a CFD study, using LES and RANS turbulence models on the wind loads and flow prediction around a standalone module of photovoltaic panels for three different tilt angles and two wind directions. The main conclusions are described below.

i. The pressure distribution, as expected, is approximately symmetrical in relation to the mid-lane on both the upper (sun-facing) and lower (ground-facing) surfaces of the panel for wind directions $\theta = 0^{o}$ and $\theta = 180^{o}$.

ii. On the upper surface, the pressure coefficient is higher at the leading edge and decreases (due to flow acceleration) towards the trailing edge to negative values for $\theta = 0^{o}$ and it is always negative at the lower surface, where suction/recirculation occurs.

iii. Maximum wind loads occur at the leading edge of the panel.

iv. Positive drag and negative lift are generated for $\theta = 0^{o}$. Moreover, drag and lift coefficients increase with tilt angle.

v. For $\theta = 180^{o}$ C_p is always negative at the upper surface decreasing from the trailing edge towards the leading edge; the lowest value is predicted at about $x/L = 0.75$. On the lower surface, C_p is always positive increasing from the trailing edge towards the leading edge.

vi. The resultant pressure coefficient for $\theta = 0^{o}$ increases with the tilt angle and has its maximum value at about $x/L = 0.3$.

vii. On the upper surface and for $\theta = 30^{o}$, the edge that is closer to the wind direction is the one that experiences the biggest pressure magnitudes while the farthest one experiences the largest negative pressure.

viii. Vortex shedding was not captured by the RANS modelling approach when compared with LES.

ix. The comparison between the numerical prediction and the experimental data showed reasonable agreement.

In summary, CFD has the potential to be an attractive tool to be integrated into the design process of solar farms as this tool reproduces results similar to experimental

measurements. Since CFD provides insight into the magnitude and distribution of wind loads it can be used to optimize the structural design and guarantee its longevity. Considering that the demand for renewable energy sources is rising rapidly this tool also has the advantage of providing results expeditiously.

When confronting the 2D and 3D results and taking into account the dynamic nature of wind loads on PV panels and their dependency on several factors, the latter possesses more arguments in favor when it comes to choosing. Regarding LES and RANS, it can be observed that the second method shows a good compromise between the accuracy of the results, execution times and computational resources.

REFERENCES

Abiola-Ogedengbe, A., Hangan, H., & Siddiqui, K. (2015). Experimental investigation of wind effects on a standalone photovoltaic (PV) module. *Renewable Energy*, *78*, 657–665. https://doi.org/10.1016/j.renene.2015.01.037

Anderson, J. (2016). *Fundamentals of Aerodynamics* (6th ed.). McGraw Hill.

Cao, J., Yoshida, A., Saha, P. K., & Tamura, Y. (2013). Wind loading characteristics of solar arrays mounted on flat roofs. *Journal of Wind Engineering and Industrial Aerodynamics*, *123*, 214–225. https://doi.org/10.1016/j.jweia.2013.08.014

Cazzaniga, R., Cicu, M., Rosa-Clot, M., Rosa-Clot, P., Tina, G. M., & Ventura, C. (2018). Floating photovoltaic plants: Performance analysis and design solutions. In *Renewable and Sustainable Energy Reviews* (Vol. 81, pp. 1730–1741). Elsevier Ltd. https://doi.org/10.1016/j.rser.2017.05.269

CFD Online. (n.d.). *Turbulence Properties, Conversions & Boundary Estimations*. https://www.cfd-online.com/Tools/turbulence.php

Chen, J. M., & Fang, Y.-C. (1996). *Strouhal numbers of inclined flat plates*.

Choi, S. M., Park, C. D., Cho, S. H., & Lim, B. J. (2022). Effects of wind loads on the solar panel array of a floating photovoltaic system – Experimental study and economic analysis. *Energy*, *256*. https://doi.org/10.1016/j.energy.2022.124649

Choi, S. M., Park, C. D., Cho, S. H., & Lim, B. J. (2023). Effects of various inlet angle of wind and wave loads on floating photovoltaic system considering stress distributions. *Journal of Cleaner Production*, *387*. https://doi.org/10.1016/j.jclepro.2023.135876

Crabtree, G. W., & Lewis, N. S. (2008). Solar Energy Conversion. *AIP Conference Proceedings*, *1044*(1), 309–321. https://doi.org/10.1063/1.2993729

Fage, A., & Johansen, F. C. (1927). Gottinger Nadir. In *Comptes Rendus* (Vol. 147). https://royalsocietypublishing.org/

Greenshields, C. J. (2022). *OpenFOAM v10 User Guide*. https://openfoam.org

Hami, K. (2021). Turbulence modeling a review for different used methods. *International Journal of Heat and Technology*, *39*(1), 227–234. https://doi.org/10.18280/ijht.390125

Hu, H. H. (2012). Computational Fluid Dynamics. *Fluid Mechanics*, 421–472. https://doi.org/10.1016/B978-0-12-382100-3.10010-1

Irtaza, H., & Agarwal, A. (2018). CFD Simulation of Turbulent Wind Effect on an Array of Ground-Mounted Solar PV Panels. *Journal of The Institution of Engineers (India): Series A*, *99*(2), 205–218. https://doi.org/10.1007/s40030-018-0283-x

Jeong, W., & Seong, J. (2014). Comparison of effects on technical variances of computational fluid dynamics (CFD) software based on finite element and finite volume methods. *International Journal of Mechanical Sciences*, *78*, 19–26. https://doi.org/10.1016/j.ijmecsci.2013.10.017

Jubayer, C. M., & Hangan, H. (2014). Wind and Thermal Effects on Ground Mounted Photovoltaic (PV) Wind and Thermal Effects on Ground Mounted Photovoltaic (PV) Panels Panels. https://ir.lib.uwo.ca/etd

Jubayer, C. M., & Hangan, H. (2015). Numerical simulation of wind effects on a stand-alone ground mounted Photovoltaic (PV) system. *Journal of Wind Engineering and Industrial Aerodynamics*, *134*, 56–64. https://doi.org/10.1016/j.jweia.2014.08.008

Kabir, E., Kumar, P., Kumar, S., Adelodun, A. A., & Kim, K. H. (2018). Solar energy: Potential and future prospects. In *Renewable and Sustainable Energy Reviews* (Vol. 82, pp. 894–900). Elsevier Ltd. https://doi.org/10.1016/j.rser.2017.09.094

Kolmogorov, A. N. (1941). The local structure of turbulence in incompressible viscous fluid for very large Reynolds number. *Cr Acad. Sci. URSS*, *30*, 301–305.

Lee, M., Park, G., Park, C., & Kim, C. (2020). Improvement of Grid Independence Test for Computational Fluid Dynamics Model of Building Based on Grid Resolution. *Advances in Civil Engineering*, *2020*. https://doi.org/10.1155/2020/8827936

Lien, F.-S., & Yee, E. (2004). Numerical modelling of the turbulent flow developing within and over a 3-d building array, part i: a high-resolution Reynolds-Averaged Navier-Stokes approach.

Markatos, N. C. (1986). The mathematical modelling of turbulent flows.

Mazzucato, M. (2015). The green entrepreneurial state. Routledge London.

Meneveau, C. (2010). Turbulence: Subgrid-Scale Modeling. *Scholarpedia*, *5*, 9489. http://www.scholarpedia.org/article/Turbulence:_Subgrid-Scale_Modeling

Menter, F. R., Kuntz, M., & Langtry, R. (2003). *Ten years of industrial experience with the SST turbulence model*. https://www.researchgate.net/publication/228742295

Moukalled, F., Mangani, L., & Darwish, M. (2016). The Finite Volume Method in Computational Fluid Dynamics (1st ed., Vol. 113).

Navier, C. (1823). Mémoire sur les lois du mouvement des fluides. *Mémoires de l'Académie Royale Des Sciences de l'Institut de France*, *6*(1823), 389–440.

Nicoud, F., & Ducros, F. (1999). *Subgrid-scale stress modelling based on the square of the velocity gradient tensor*.

Nozaki, F. (2016, December 9). Smagorinsky SGS model in OpenFOAM. https://caefn.com/openfoam/smagorinsky-sgs-model

Oliveira, L. A., & Lopes, A. G. (2016). Mecânica Dos Fluídos (5.ª Edição).

Pfahl, A., Buselmeier, M., & Zaschke, M. (2011). Wind loads on heliostats and photovoltaic trackers of various aspect ratios. *Solar Energy*, *85*(9), 2185–2201. https://doi.org/10.1016/j.solener.2011.06.006

Pieris, S., Yarusevych, S., & Peterson, S. D. (2022). Flow development over inclined flat plates in ground effect and relation to aerodynamic loads. *Physics of Fluids*, *34*(9). https://doi.org/10.1063/5.0102406

Piomelli, U. (1999). Large-eddy simulation: achievements and challenges. In *Progress in Aerospace Sciences* (Vol. 35).

Piomelli, U. (2014). Large eddy simulations in 2030 and beyond. *Philosophical Transactions of the Royal Society A: Mathematical, Physical and Engineering Sciences*, *372*(2022). https://doi.org/10.1098/rsta.2013.0320

Reina, G. P., & De Stefano, G. (2017). Computational evaluation of wind loads on sun-tracking ground-mounted photovoltaic panel arrays. *Journal of Wind Engineering and Industrial Aerodynamics*, *170*, 283–293. https://doi.org/10.1016/j.jweia.2017.09.002

Shademan, M., Balachandar, R., & Barron, R. M. (2014). Detached eddy simulation of flow past an isolated inclined solar panel. *Journal of Fluids and Structures*, *50*, 217–230. https://doi.org/10.1016/j.jfluidstructs.2014.06.024

Smits, A. J. (2009). Lectures in Fluid Mechanics Viscous Flows and Turbulence.

Sreenivasan, K. R. (1999). Fluid turbulence.

Stathopoulos, T., Zisis, I., & Xypnitou, E. (2014). Local and overall wind pressure and force coefficients for solar panels. *Journal of Wind Engineering and Industrial Aerodynamics*, *125*, 195–206. https://doi.org/10.1016/j.jweia.2013.12.007

Stokes, G. G. (1845). On the theories of the internal friction of fluids in motion, and of the equilibrium and motion of pendulums. *Trans. Camb. Phil. Soc*.

Strobel, K., & Banks, D. (2014). Effects of vortex shedding in arrays of long inclined flat plates and ramifications for ground-mounted photovoltaic arrays. *Journal of Wind Engineering and Industrial Aerodynamics*, *133*, 146–149. https://doi.org/10.1016/j.jweia.2014.06.013

Sumner, J., Watters, C. S., & Masson, C. (2010). CFD in wind energy: The virtual, multiscale wind tunnel. In *Energies* (Vol. 3, Issue 5, pp. 989–1013). MDPI AG. https://doi.org/10.3390/en3050989

Uematsu, Y., Yambe, T., & Yamamoto, A. (2022). Application of a Numerical Simulation to the Estimation of Wind Loads on Photovoltaic Panels Installed Parallel to Sloped Roofs of Residential Houses. *Wind*, *2*(1), 129–149. https://doi.org/10.3390/wind2010008

Versteeg, H. K., & Malalasekera, W. (2007). An introduction to computational fluid dynamics: the finite volume method (Second). Pearson education.

Wang, J., Van Phuc, P., Yang, Q., & Tamura, Y. (2020). LES study of wind pressure and flow characteristics of flat-roof-mounted solar arrays. *Journal of Wind Engineering and Industrial Aerodynamics*, *198*. https://doi.org/10.1016/j.jweia.2020.104096

Warsido, W. P., Bitsuamlak, G. T., Barata, J., & Gan Chowdhury, A. (2014). Influence of spacing parameters on the wind loading of solar array. *Journal of Fluids and Structures*, *48*, 295–315. https://doi.org/10.1016/j.jfluidstructs.2014.03.005

Wilcox, D. C. (1988). Reassessment of the scale-determining equation for advanced turbulence models. *AIAA Journal*, *26*(11), 1299–1310.

Wittwer, A. R., Podestá, J. M., Castro, H. G., Mroginski, J. L., Marighetti, J. O., De Bortoli, M. E., Paz, R. R., & Mateo, F. (2022). Wind loading and its effects on photovoltaic modules: An experimental–Computational study to assess the stress on structures. *Solar Energy*, *240*, 315–328. https://doi.org/10.1016/j.solener.2022.04.061

Yusof, S. N. A., Asako, Y., Sidik, N. A. C., Mohamed, S. B., & Japar, W. M. A. A. (2020). A short review on rans turbulence models. In *CFD Letters* (Vol. 12, Issue 11, pp. 83–96). Penerbit Akademia Baru. https://doi.org/10.37934/cfdl.12.11.8396

Zhiyin, Y. (2015). Large-eddy simulation: Past, present and the future. In *Chinese Journal of Aeronautics* (Vol. 28, Issue 1, pp. 11–24). Chinese Journal of Aeronautics. https://doi.org/10.1016/j.cja.2014.12.007

APPENDIX A – BOUNDARY CONDITIONS DICTIONARIES

```
/*--------------------------------*- C++ -*----------------------------------*\
  =========                 |
  \\      /  F ield         | OpenFOAM: The Open Source CFD Toolbox
   \\    /   O peration     | Website:  https://openfoam.org
    \\  /    A nd           | Version:  10
     \\/     M anipulation  |
\*---------------------------------------------------------------------------*/
FoamFile
{
    format      ascii;
    class       volScalarField;
    object      k;
}
// * * * * * * * * * * * * * * * * * * * * * * * * * * * * * * * * * * * * * //


dimensions      [0 2 -2 0 0 0 0];

internalField   uniform 0.008664000000000002;

boundaryField
{

    inlet
    {
        type            fixedValue;
        value           uniform 0.008664000000000002;
    }
    outlet
    {
        type            zeroGradient;
    }

    lowerWall
    {
        type            kqRWallFunction;
        value           uniform 1e-8;
    }

    standalonePanel
    {
        type            kqRWallFunction;
        value           uniform 1e-8;
    }

    upperWall
    {
        type            slip;
    }

    frontAndBack
    {
        type            slip;
    }
}


// ************************************************************************* //
```

```
/*--------------------------------*- C++ -*----------------------------------*\
  =========                 |
  \\      /  F ield         | OpenFOAM: The Open Source CFD Toolbox
   \\    /   O peration     | Website:  https://openfoam.org
    \\  /    A nd           | Version:  10
     \\/     M anipulation  |
\*---------------------------------------------------------------------------*/
FoamFile
{
    format      ascii;
    class       volVectorField;
    object      U;
}
// * * * * * * * * * * * * * * * * * * * * * * * * * * * * * * * * * * * * * //

dimensions      [0 1 -1 0 0 0 0];

internalField   uniform (0.76 0 0);

boundaryField
{
    inlet
    {
        type        fixedProfile;
        profile     tableFile;
        file        "0/perfilVelocidade3D.csv";
        format csv;
        nHeaderLine 1;
        refColumn 0;
        componentColumns 3(1 2 3);
        separator ";";
        mergeSeparators 0;
        interpolationScheme linear;
        direction (0 1 0);
        origin 0;
    }
    outlet
    {
        type            zeroGradient;
    }
    frontAndBack
    {
        type            slip;
    }
    lowerWall
    {
        type            noSlip;
    }
    upperWall
    {
        type            slip;
    }
    standalonePanel
    {
        type            noSlip;
    }
}

// ************************************************************************* //
```

```
/*--------------------------------*- C++ -*----------------------------------*\
  =========                 |
  \\      /  F ield         | OpenFOAM: The Open Source CFD Toolbox
   \\    /   O peration     | Website:  https://openfoam.org
    \\  /    A nd           | Version:  10
     \\/     M anipulation  |
\*---------------------------------------------------------------------------*/
FoamFile
{
    format      ascii;
    class       volScalarField;
    object      omega;
}
// * * * * * * * * * * * * * * * * * * * * * * * * * * * * * * * * * * * * * //


dimensions      [0 0 -1 0 0 0 0];

internalField   uniform 0.04654030511288038;

boundaryField
{
    inlet
    {
        type            fixedValue;
        value           uniform 0.04654030511288038;
    }
    outlet
    {
        type            zeroGradient;
    }
    lowerWall
    {
        type            omegaWallFunction;
        value           uniform 0.04654030511288038;
    }
    standalonePanel
    {
        type            omegaWallFunction;
        value           uniform 275135;  // Equation (4.6)
    }
    upperWall
    {
        type            slip;
    }
    frontAndBack
    {
        type            slip;

    }
}


// ************************************************************************* //
```

```
/*--------------------------------*- C++ -*----------------------------------*\
  =========                 |
  \\      /  F ield         | OpenFOAM: The Open Source CFD Toolbox
   \\    /   O peration     | Website:  https://openfoam.org
    \\  /    A nd           | Version:  10
     \\/     M anipulation  |
\*---------------------------------------------------------------------------*/
FoamFile
{
    format      ascii;
    class       volScalarField;
    object      p;
}
// * * * * * * * * * * * * * * * * * * * * * * * * * * * * * * * * * * * * * //


dimensions      [0 2 -2 0 0 0 0];

internalField   uniform 0;

boundaryField
{
    inlet
    {
        type            zeroGradient;
    }
    outlet
    {
        type            fixedValue;
        value           uniform 0;
    }
    lowerWall
    {
        type            zeroGradient;
    }
    standalonePanel
    {
        type            zeroGradient;
    }
    upperWall
    {
        type        zeroGradient;
    }
    frontAndBack
    {
        type        zeroGradient;
    }
}

// ************************************************************************* //
```

APPENDIX B – 3D FLOW STREAMLINES

Screenshots taken from the post processing software regarding the streamlines are shown in order, that is from 25º to 40º. The latter figures are the representation for $\theta = 180º$ and $\theta = 30º$.

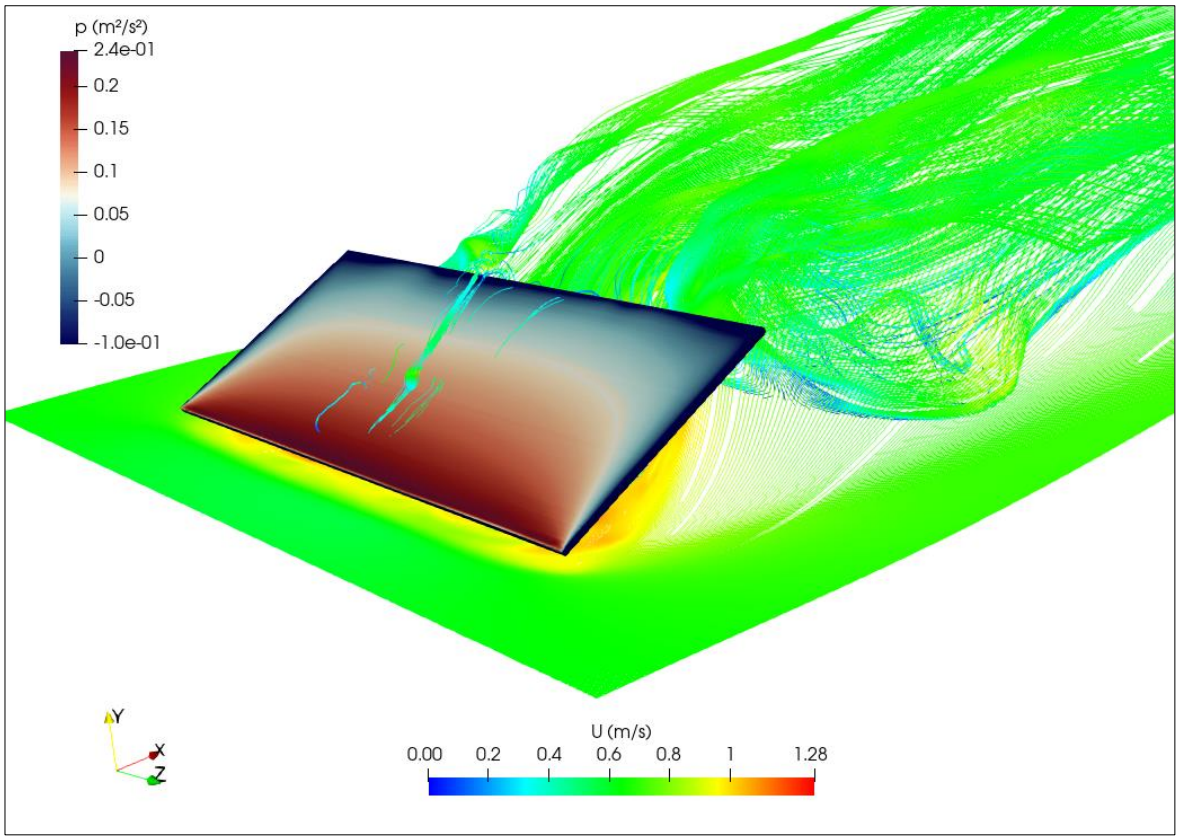

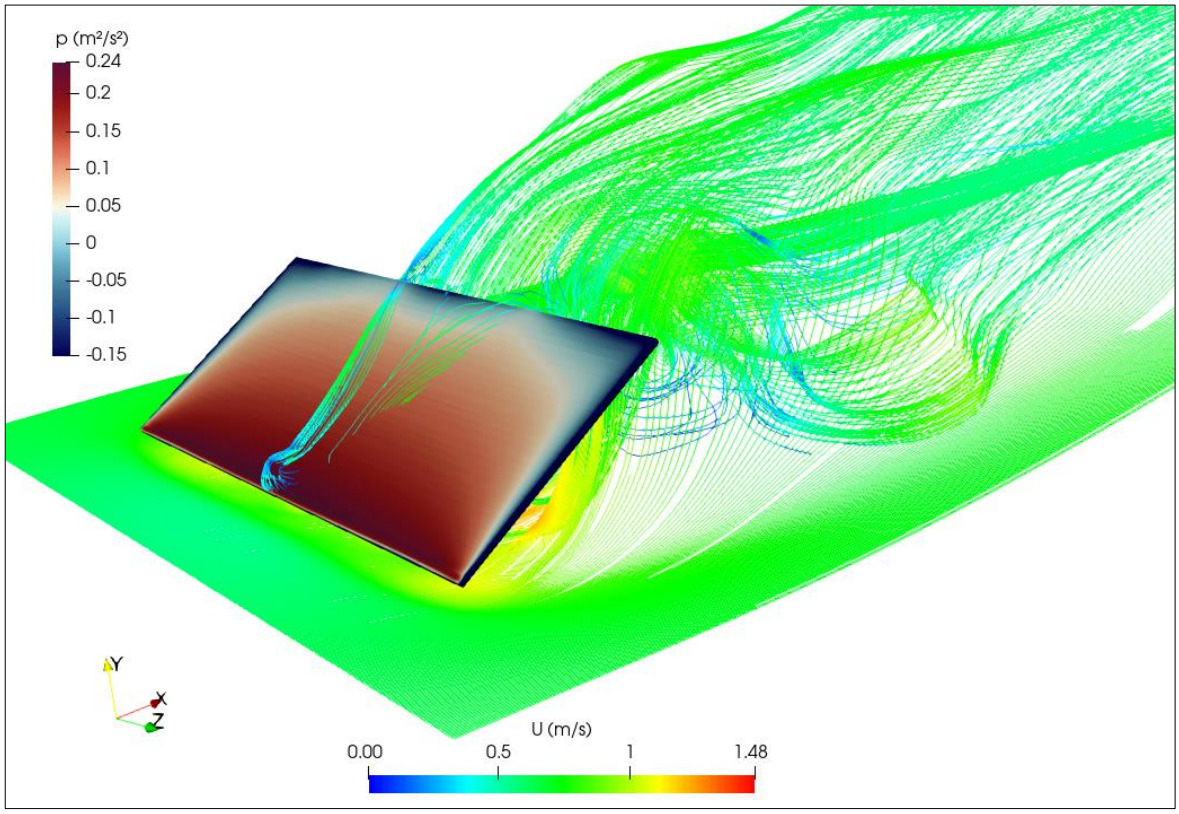
p (m²/s²)
0.24
0.2
0.15
0.1
0.05
0
-0.05
-0.1
-0.15
Y
X
Z
U (m/s)
0.00
0.5
1
1.48

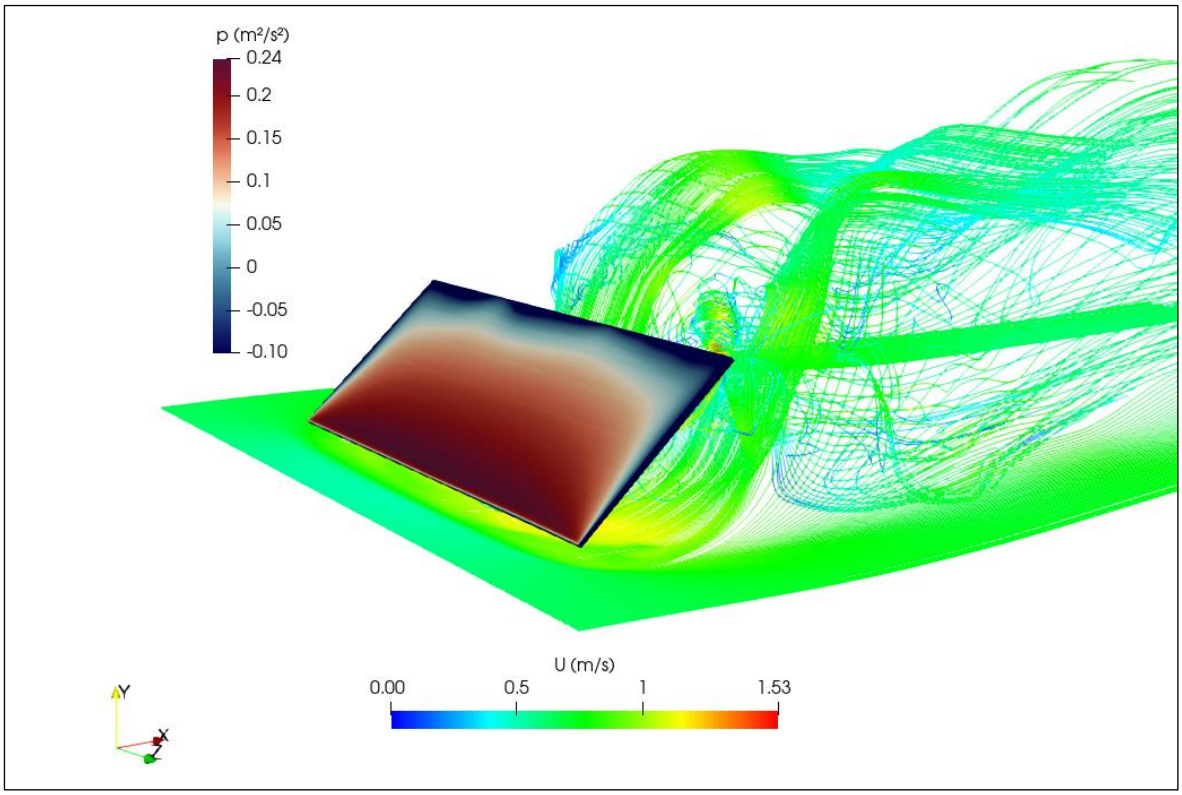
p (m²/s²)
0.24
0.2
0.15
0.1
0.05
0
-0.05
-0.10
Y
X
Z
U (m/s)
0.00
0.5
1
1.53

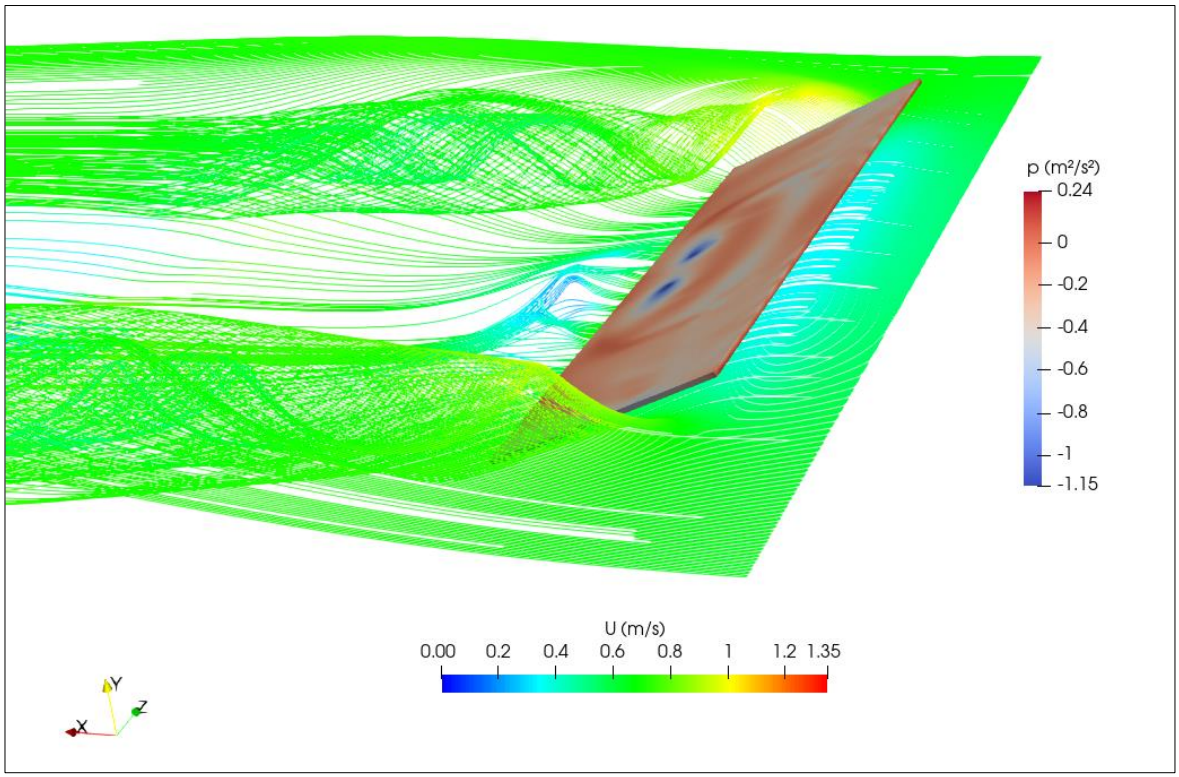
p (m²/s²)
0.24
0
-0.2
-0.4
-0.6
-0.8
-1
-1.15
U (m/s)
0.00 0.2 0.4 0.6 0.8 1 1.2 1.35
Y
Z
X

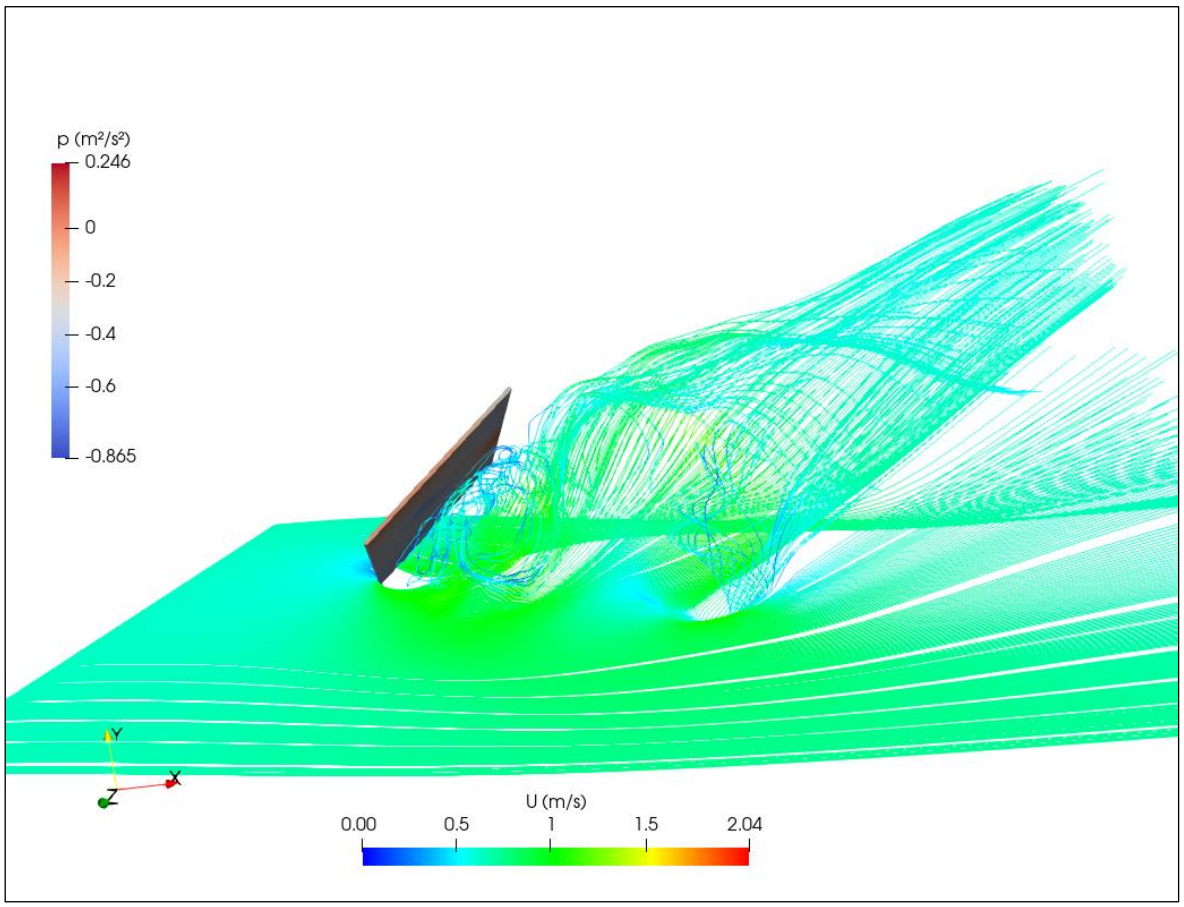
p (m²/s²)
0.246
0
-0.2
-0.4
-0.6
-0.865
U (m/s)
0.00 0.5 1 1.5 2.04
Y
X
Z